Rapid ductile strain localization due to thermal runaway

A. Spang [1], M. Thielmann [1,2], D. Kiss [3,4]

[1]Bayerisches Geoinstitut, Universität Bayreuth, Bayreuth, Germany
[2]Institut für Geowissenschaften, Christian-Albrechts-Universität Kiel, Kiel, Germany
[3]Institut für Geowissenschaften, Johannes Gutenberg-Universität Mainz, Mainz, Germany
[4]Department of Reservoir Technology, Institute for Energy Technology, Kjeller, Norway

Key Points:

- Numerical investigation of thermal runaway in visco-elastic material with diffusion creep, dislocation creep and low-temperature plasticity
- Nondimensional scaling analysis reveals two dimensionless groups governing the occurrence of thermal runaway
- Ductile localization can cause slip events in line with deep earthquakes and pseudotachylyte formation at subducting slab core conditions

Corresponding author: Arne Spang, `arne.spang@uni-bayreuth.de`

Abstract

Thermal runaway is a ductile localization mechanism that has been linked to deep-focus earthquakes and pseudotachylyte formation. In this study, we investigate the dynamics of this process using one-dimensional, numerical models of simple shear deformation. The models employ a visco-elastic rheology where viscous creep is accommodated with a composite rheology encompassing diffusion and dislocation creep as well as low-temperature plasticity. To solve the nonlinear system of differential equations governing this rheology, we utilize the pseudo-transient iterative method in combination with a viscosity regularization to avoid resolution dependencies. To determine the impact of different model parameters on the occurrence of thermal runaway, we perform a parameter sensitivity study consisting of 6000 numerical experiments. We observe two distinct behaviors, namely a stable regime, characterized by transient shear zone formation accompanied by a moderate (100 - 300 Kelvin) temperature increase, and a thermal runaway regime, characterized by strong localization, rapid slip and a temperature surge of thousands of Kelvin. Nondimensional scaling analysis allows us to determine two dimensionless groups that predict model behavior. The ratio $t_\mathrm{r}/t_\mathrm{d}$ represents the competition between heat generation from stress relaxation and heat loss due to thermal diffusion while the ratio $U_\mathrm{el}/U_\mathrm{th}$ compares the stored elastic energy to thermal energy in the system. Thermal runaway occurs if $t_\mathrm{r}/t_\mathrm{d}$ is small and $U_\mathrm{el}/U_\mathrm{th}$ is large. Our results demonstrate that thermal runaway is a viable mechanism driving fast slip events that are in line with deep-focus earthquakes and pseudotachylyte formation at conditions resembling cores of subducting slabs.

Plain Language Summary

Thermal runaway is a mechanism that concentrates material deformation into thin layers without breaking the material and has been linked to earthquakes more than 70 km below the surface. This study uses one-dimensional computer models with a complex material behavior and conducts 6000 numerical experiments to investigate the influence of different parameters like temperature, deformation rate and material properties. Results show two distinct behaviors, namely a stable regime with slow sliding and a temperature rise of 100 - 300 Kelvin or thermal runaway with fast movement and a temperature increase of a few thousand Kelvin. We find two dimensionless ratios that are combinations of the input parameters and can predict the behavior. The ratio $t_\mathrm{r}/t_\mathrm{d}$ compares heat production to heat loss, and the ratio $U_\mathrm{el}/U_\mathrm{th}$ compares stored elastic en-

ergy to thermal energy. If the first ratio is small and the second ratio is large, thermal runaway occurs. Our results show that thermal runaway could cause fast deformation events like earthquakes and produce thin layers of molten rock in conditions that are typical for some locations inside the Earth.

Index Terms

0545 Modeling
1906 Computational models, algorithms
4445 Nonlinear differential equations
5120 Plasticity, diffusion, and creep
7209 Earthquake dynamics

Keywords

Ductile localization, Thermal runaway, Pseudo-Transient, Nondimensional scaling, Deep earthquakes, Viscosity regularization

1 Introduction

Strain localization characterizes geodynamic processes across scales ranging from μm (mineral grains) to thousands of km (plate tectonics) by allowing "stiff" blocks to move past each other on thin, "weak" layers. In the crust, this usually occurs via brittle failure (i.e., breaking the rock). As brittle strength is expected to increase linearly with confining pressure (Byerlee, 1978) until reaching the strength of atomic bonds (Renshaw & Schulson, 2007), a ductile localization process is likely dominant at larger depths.

Alongside grain size reduction (e.g., Kameyama et al., 1997; Braun et al., 1999; Ricard & Bercovici, 2009; Thielmann et al., 2015), a commonly proposed mechanism for ductile localization is viscous dissipation or shear heating (e.g., Brinkman, 1951; Yuen et al., 1978; Regenauer-Lieb & Yuen, 1998). The combination of deformation, shear heating and a temperature-dependent rheology form a positive feedback loop called thermal runaway that can lead to catastrophic strain localization and fast-slip events (Gruntfest, 1963; Hobbs et al., 1986). Thermal runaway has been linked to lithosphere-scale deformation (e.g., Regenauer-Lieb & Yuen, 2004; Kaus & Podladchikov, 2006; Thielmann &

Kaus, 2012; Kiss et al., 2019) and deep-focus earthquakes (e.g., Ogawa, 1987; Regenauer-Lieb & Yuen, 2003; John et al., 2009; Thielmann et al., 2015).

A number of previous one-dimensional (1D) studies have numerically investigated ductile localization and/or thermal runaway with varying rheological complexity ranging from diffusion creep to nonlinear visco-elasticity including grain size evolution (e.g., Yuen et al., 1978; Ogawa, 1987; Braun et al., 1999; Kaus & Podladchikov, 2006; Braeck et al., 2009; Thielmann et al., 2015). Kameyama et al. (1999) and Thielmann (2018) are the only studies to include low-temperature plasticity (LTP) in their rheological model, concluding that it inhibits or delays thermal runaway at natural conditions. While all studies observe ductile localization, an important distinction can be made between localization onto finite width shear zones accompanied by moderate temperature increases (100 - 300 K) towards a quasi-steady-state (e.g., Yuen et al., 1978; Kiss et al., 2019) and infinite-like localization accompanied by temperature increases of several hundreds or thousands of Kelvin within seconds (e.g., Ogawa, 1987; Braeck et al., 2009). We will only refer to the latter case as thermal runaway. While successful two- and three-dimensional (2D and 3D) models of ductile localization exist (e.g., Kaus & Podladchikov, 2006; Duretz et al., 2019; Kiss et al., 2019), extensive parameter studies are limited to 1D due to the large computational cost of 2D and 3D simulations.

The aims of our study are as follows: (i) develop a 1D numerical code that can cover the loading, heating and unloading (through shear zones and/or thermal runaway) of rock with a rheology including elasticity, diffusion creep, dislocation creep and low-temperature plasticity, (ii) present numerical strategies to deal with nonlinearities during thermal runaway, (iii) illustrate the effects of such strategies, (iv) identify the necessary conditions for thermal runaway in velocity driven simple shear.

2 Methods

Section 2.1 presents the model setup, section 2.2 lists the governing equations and section 2.3 outlines their implementation. Section 2.4 outlines the ranges of our parameter study.

2.1 Model setup

We use a 1D simple shear setup with an olivine rheology, a central, weak anomaly and constant kinematic boundary conditions that load the model (Fig. 1a). The anomaly is created by multiplying the diffusion and dislocation creep flow law pre-factors by a vector ω which follows a normal distribution, centered at 0, with a minimum of 1, a maximum of $\omega_0 > 1$ and a full-width-half-maximum (FWHM) of h:

$$\omega = 1 + (\omega_0 - 1)\ e^{-\frac{1}{2}\left(\frac{x}{\sigma}\right)^2}, \tag{1}$$

where

$$\sigma = \frac{h}{\sqrt{8\ln(2)}}, \tag{2}$$

and x is the coordinate vector. The lower domain boundary is no-slip and the upper edge is moving with a fixed velocity (V_{top}). Both boundaries are thermally insulated (i.e., no heat flux).

2.2 Governing equations

The system described above is governed by the equations

$$\frac{\partial \tau}{\partial x} = 0, \tag{3}$$

$$\rho C_p \frac{dT}{dt} = \lambda \frac{\partial^2 T}{\partial x^2} + \tau \dot{\varepsilon}_{\mathrm{vi}}, \tag{4}$$

$$\dot{\varepsilon} = \frac{1}{2}\frac{\partial V}{\partial x}, \tag{5}$$

where τ is the shear stress (xy-component of the Cauchy stress deviator), x is the spatial dimension, ρ the density, C_p the specific heat capacity, T the temperature, t the time, λ the thermal conductivity, $\dot{\varepsilon}$ the shear component of the deviatoric strain rate, $\dot{\varepsilon}_{\mathrm{vi}}$ its viscous part and V the velocity perpendicular to the spatial dimension. All other components of the stress and strain rate tensor and velocity vector are equal to zero. This implies that the divergence of velocity is zero and the system incompressible. For simplicity, we neglect inertia and body forces (i.e., gravity) as well as adiabatic and radio-

genic heating. The last term of equation (4) represents heat generation by viscous dissipation.

We describe the visco-elastic rheology via a Maxwell model:

$$\dot{\varepsilon} = \dot{\varepsilon}_{\mathrm{el}} + \dot{\varepsilon}_{\mathrm{vi}} = \frac{1}{2\,G}\frac{d\tau}{dt} + \frac{\tau}{2\,\eta}, \tag{6}$$

where $\dot{\varepsilon}_{\mathrm{el}}$ and $\dot{\varepsilon}_{\mathrm{vi}}$ are the elastic and viscous components of the deviatoric strain rate, G the shear modulus and η the effective viscosity.

2.3 Implementation

We discretize equations (3)-(6) with finite differences on a staggered grid where material parameters, pressure, temperature, stress and strain rate are defined on cell centers and velocities on cell edges (e.g., Gerya & Yuen, 2003). Equations are solved using the damped psuedo-transient approach (e.g, Frankel, 1950; Duretz et al., 2019; Räss et al., 2022). The code is written in the Julia programming language and we utilize the package GeoParams.jl (Kaus et al., 2023) for internal nondimensionalization and scaling.

2.3.1 Pseudo-transient approach

In the pseudo-transient approach, the conservation equations are solved at every physical time step by introducing a residual (or pseudo time derivative) for each equation and iteratively incrementing the primary variables V and T until the residuals are smaller than a given numerical tolerance. Applying this procedure to equations (3) and (4) yields

$$\frac{\partial V}{\partial \psi} = \frac{\partial \tau}{\partial x}, \tag{7}$$

$$\frac{\partial T}{\partial \psi} = \frac{\lambda \frac{\partial^2 T}{\partial x^2} + \tau\,\dot{\varepsilon}_{\mathrm{vi}}}{\rho C_p} - \frac{dT}{dt}, \tag{8}$$

where $\frac{\partial}{\partial \psi}$ denotes the residual or evolution in pseudo-time. During each pseudo-time iteration, each primary variable is incremented proportional to the sum of the current residual and the previous increment (Duretz et al., 2019).

$$\Delta_\gamma = \left[\frac{\partial \gamma}{\partial \psi} + \left(1 - \frac{1}{\zeta_\gamma}\right) \Delta_\gamma^{\text{prev}}\right] \Delta\psi_\gamma, \tag{9}$$

where γ is either V or T, Δ_γ is the increment to the respective variable, $\Delta_\gamma^{\text{prev}}$ is the increment of the previous iteration, ζ_γ is the damping parameter (> 1) and $\Delta\psi_\gamma$ is the size of the pseudo time step.

2.3.2 Rheology and density

Viscous deformation is a combination of diffusion creep, dislocation creep and low-temperature plasticity:

$$\dot{\varepsilon}_{\text{vi}} = \dot{\varepsilon}_{\text{dif}} + \dot{\varepsilon}_{\text{dis}} + \dot{\varepsilon}_{\text{LTP}}, \tag{10}$$

where the subscripts $_{\text{dif}}$, $_{\text{dis}}$ and $_{\text{LTP}}$ denote diffusion creep, dislocation creep and low-temperature plasticity respectively. Consequently, the effective viscosity η can be expressed as

$$\eta = \left(\frac{1}{\eta_{\text{dif}}} + \frac{1}{\eta_{\text{dis}}} + \frac{1}{\eta_{\text{LTP}}}\right)^{-1}, \tag{11}$$

$$\eta_{\text{dif}} = \frac{1}{2} A_{\text{dif}}^{-1}\, d^m\, e^{\frac{E_{\text{dif}}}{RT}}, \tag{12}$$

$$\eta_{\text{dis}} = \frac{1}{2} (A_{\text{dis}})^{-\frac{1}{n}}\, (\dot{\varepsilon}_{\text{dis}})^{\frac{1}{n}-1}\, e^{\frac{E_{\text{dis}}}{nRT}}, \tag{13}$$

$$\eta_{\text{LTP}} = \frac{\sigma_{\text{LTP}}}{2\,\dot{\varepsilon}_{\text{LTP}}}, \tag{14}$$

where A are pre-factors and E are activation energies of the respective flow laws, d is the grain size, m the grain size exponent of diffusion creep, R the universal gas constant and n the powerlaw exponent of dislocation creep. The LTP-stress σ_{LTP} is given by

$$\sigma_{\text{LTP}} = \frac{RT}{E_{\text{LTP}}}\, \sigma_{\text{res}}\, \sinh^{-1}\left(\frac{\dot{\varepsilon}_{\text{II}}^{\text{LTP}}}{A_{\text{LTP}}} e^{\frac{E_{\text{LTP}}}{RT}}\right) + \sigma_{\text{b}}, \tag{15}$$

$$\sigma_{\text{res}} = \sigma_{\text{L}} + \frac{\sigma_{\text{K}}}{\sqrt{d}}, \tag{16}$$

where σ_{b}, σ_{L} and σ_{K} are material constants (Hansen et al., 2019). Given the non-linear nature of dislocation creep and low-temperature plasticity, the strain rate partitioning (eq. (10)) can not be solved analytically, but requires an iterative approach. It

can be updated and solved alongside the conservation equations (eq. (7) and (8)). Once the left hand side terms in equations (7) and (8), as well as the residual of equation (6) are smaller than the tolerance, the solution is converged and is equivalent to a fully implicit, backward Euler solution with converged non-linearities.

Figure 1b shows a deformation mechanism map for the rheological model described by equations (10)-(16) and illustrates that LTP dominates at low temperatures, diffusion creep at high temperatures and dislocation creep at high strain rates due its shear thinning nature. The values of all used material parameters are given by Table 1.

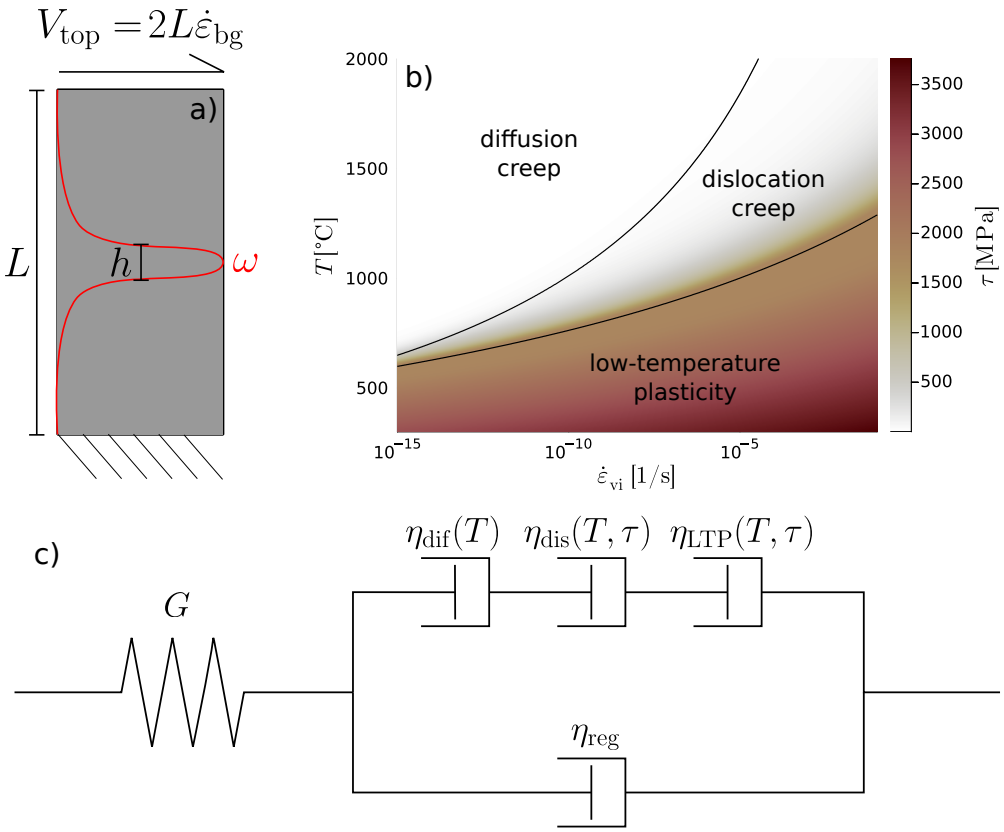

Figure 1. Model setup and rheology. (a) 1D Model setup including boundary conditions. h and L are not to scale. (b) Deformation mechanism map for our rheological model. (c) Illustration of the individual components of the rheological model. η_{reg} is purely numerical and facilitates stability during the runaway when the upper viscosity branch trends towards 0.

As we are focused on understanding the impact of the composite creep rheology, we do not include grain size evolution in our model. In addition, there is no experimen-

Table 1. Material parameters. Diffusion and dislocation creep are for dry olivine from (Hirth & Kohlstedt, 2003) and low-temperature plasticity from (Hansen et al., 2019). Values with ranges were varied with the default value in parenthesis.

Parameter		Value
G	[GPa]	40 - 160 (80)
m		3
A_{dif}	$[\mu\mathrm{m}^{\mathrm{m}}\,\mathrm{MPa}^{-1}\,\mathrm{s}^{-1}]$	1.5×10^9
E_{dif}	$[\mathrm{kJ\,mol}^{-1}]$	375
d	$[\mu\mathrm{m}]$	100
n		3.5
A_{dis}	$[\mathrm{MPa}^{-\mathrm{n}}\,\mathrm{s}^{-1}]$	1.1×10^5
E_{dis}	$[\mathrm{kJ\,mol}^{-1}]$	530
A_{LTP}	$[\mathrm{s}^{-1}]$	5×10^{20}
E_{LTP}	$[\mathrm{kJ\,mol}^{-1}]$	550
σ_{L}	[GPa]	3.1
σ_{K}	$[\mathrm{GPa}\,\mu\mathrm{m}^{0.5}]$	3.2
σ_{b}	[GPa]	0.9 - 2.7 (1.8)
P_0	[GPa]	10
ρ_0	$[\mathrm{kg\,m}^{-3}]$	3300
C_p	$[\mathrm{J\,kg}^{-1}\,\mathrm{K}^{-1}]$	1000
λ	$[\mathrm{J\,s}^{-1}\,\mathrm{m}^{-1}\,\mathrm{K}^{-1}]$	0.75 - 12 (3)

tal data on the contribution of LTP to grain size evolution. Even for dislocation creep, the partitioning factor of dissipative work is a controversial topic spanning several orders of magnitude in different studies (Chrysochoos & Belmahjoub, 1992; Austin et al., 2008; Rozel et al., 2011; Mulyukova & Bercovici, 2017; Holtzman et al., 2018; Ruh et al., 2022).

We assume a background pressure $P_0 = 10$ GPa which is roughly equivalent to 300 km depth and a Poisson's ratio of $\nu = 0.25$ to adjust density (ρ) to upper mantle conditions.

$$\rho = \rho_0 \, e^{\frac{P_0}{K_\mathrm{b}}}, \tag{17}$$

$$K_\mathrm{b} = \frac{2\,G\,(1+\nu)}{3\,(1-2\,\nu)}. \tag{18}$$

2.3.3 Regularization

Once initiated, the feedback loop of thermal runaway has no self-limiting mechanism other than heat diffusion. In viscous models, thermal diffusion can limit localization to a finite width (Duretz et al., 2014; Kiss et al., 2019). However, for visco-elastic rheologies, deformation commonly localizes onto a single grid cell which leads to mesh-dependent results (e.g., Iordache & Willam, 1998; De Borst et al., 1993; Jacquey et al., 2021) and temperatures of several tens of thousands °C (e.g., Ogawa, 1987; Thielmann et al., 2015). This poses several challenges: (i) The temperature rise is unrealistic as it would naturally be inhibited by melting. (ii) Computed velocities depend on spatial resolution. (iii) The solution is numerically unstable as equation (11) approaches zero at high temperatures.

To deal with the aforementioned issues, we regularize the viscous components of our rheological model (Fig. 1c), effectively adding a term to equation (11) which yields

$$\eta = \left(\frac{1}{\eta_\mathrm{dif}} + \frac{1}{\eta_\mathrm{dis}} + \frac{1}{\eta_\mathrm{LTP}} \right)^{-1} + \eta_\mathrm{reg}. \tag{19}$$

This approach has also been used to regularize brittle plasticity (e.g., Duretz et al., 2020; Jacquey & Cacace, 2020; Kiss et al., 2023). In section 3.2, we demonstrate how η_reg affects stress evolution, maximum velocity and maximum temperature. We furthermore show how it introduces a grid independent length scale into the thickness of the shear zone.

2.3.4 Discretization

During thermal runaway, temperature, stress and velocity change drastically, thus requiring physical time steps in the range of milliseconds. The loading phase does, however, require time steps of hundreds of years. To address this issue, we employ an adaptive time-stepping scheme which adjusts the physical time step depending on the maximum temperature and stress change in the model. To maximize the resolution in the

area where runaway is expected, we employ a variable grid spacing where cell size linearly increases from the center to the outside. The outermost cells are about 125 times as large as the innermost ones.

2.4 Parameter study

We conduct 6000 numerical experiments, varying the parameters $\dot{\varepsilon}_{\mathrm{bg}}$, G, σ_{b}, L, λ, T_0, ω_0 and h/L. The ranges for each parameter is given by Table 2. Temperatures are typical for the cores of subducting slabs (e.g., Gasc et al., 2022). Simulations run until they reach a shear strain of 1 which equates to a simulation time of 6 - 3000 kyr depending on $\dot{\varepsilon}_{\mathrm{bg}}$. All models use $\eta_{\mathrm{reg}} = 10^{12}\,\mathrm{Pa\,s}$ as this introduces no significant changes in the stress evolution, while improving convergence and limiting temperatures (see section 3.2). In supplementary Table S1, we show the full list of input parameter combinations.

Table 2. Model parameter ranges.

	$\dot{\varepsilon}_{\mathrm{bg}}\,[\mathrm{s}^{-1}]$	$G\,[\mathrm{GPa}]$	$\sigma_{\mathrm{b}}\,[\mathrm{GPa}]$	$L\,[\mathrm{km}]$	$\lambda\,[\mathrm{J\,s^{-1}\,m^{-1}\,K^{-1}}]$	$T_0\,[^\circ\mathrm{C}]$	ω_0	h/L
Min	1×10^{-14}	40	0.9	1	0.75	550	1.01	0.005
Max	5×10^{-12}	160	2.7	180	12	750	100	0.080

3 Results

3.1 General behavior

In Figure 2, we show the temporal evolution of stress and maximum temperature in four representative simulations. Some models exhibit low-temperature plasticity and thermal runaway (Figure 2a), some show runaway without LTP (Figure 2b), some exhibit LTP without runaway (Figure 2c) and other simulations exhibit neither process (Figure 2d). Each model starts with a phase of elastic loading where stress increases linearly until viscous creep limits and/or releases it. If models reach the low-temperature plasticity limit σ_{LTP} (Figure 2a,c), the temperature then starts to rise due to shear heating until stresses relax (black crosses in Figure 2) which is accompanied by a steeper temperature increase. At larger initial temperatures, relaxation starts before σ_{LTP} is reached (Figure 2b,d).

In all cases, we observe two types of behavior once stress relaxation starts. (i) Stress is relaxed over tens of thousands of years, accompanied by a temperature rise of 100 to 300 Kelvin (Figure 2c,d). (ii) Stress is relaxed within seconds, accompanied by a temperature surge of up to thousands of Kelvin and a large slip event in the central anomaly (i.e., thermal runaway occurs, Figure 2a,b). Runaway may be preceded by a phase of slow relaxation (Figure 2b) or occur immediately after relaxation starts (Figure 2a).

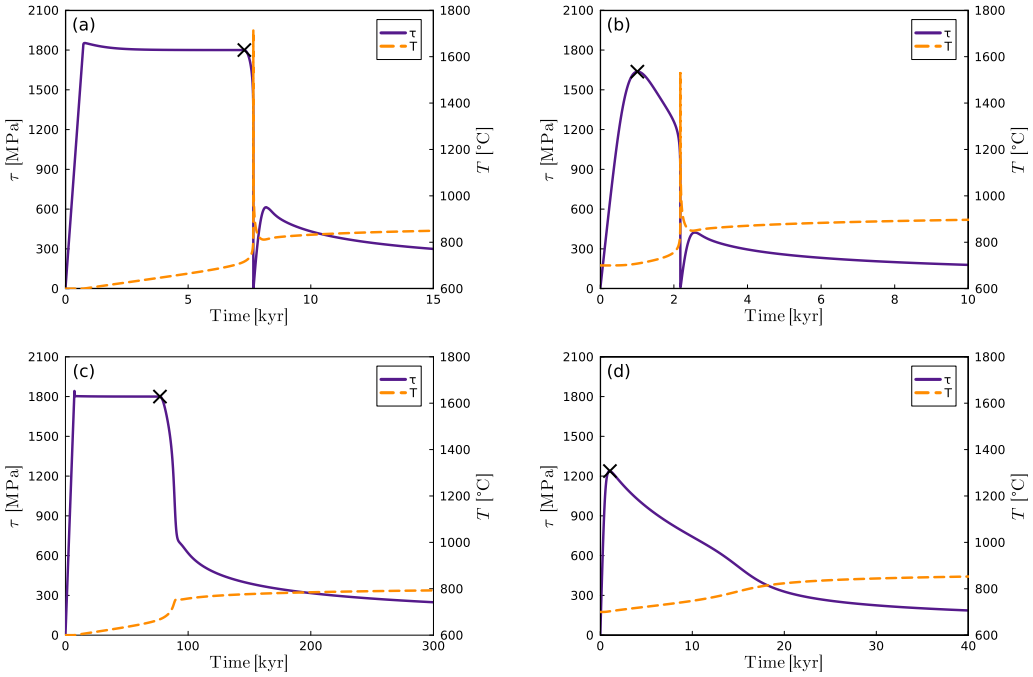

Figure 2. Stress and maximum temperature evolution for representative cases. Models in the left column reached σ_{LTP}, models in the right column did not. (a,b) Thermal runaway occurs, stresses are relaxed quickly with a large temperature surge. (c,d) No thermal runaway occurs, stresses are relaxed with a moderate temperature rise.

In Figure 3, we show the evolution of stress and maximum temperature (3a), velocity (3b), viscous dissipation (3c) and location on the deformation mechanism map (3d) in a runaway case. While stress is at the LTP-limit, heating occurs mainly due to low-temperature plasticity and the velocity profile is linear. Once dislocation creep takes over inside the anomaly (orange cross in Figure 3), deformation starts to localize in the center and stress decreases. Afterwards, the model enters thermal runaway. During this phase, viscous dissipation of diffusion and dislocation creep increase by about 6 orders of mag-

nitude, resulting in a slip event in the center (inset in Figure 3b). During the peak of the runaway, diffusion creep shortly becomes the dominant mechanism. As heat subsequently diffuses from the slip zone into the host rock, stress increases again and the model enters a stable sliding regime governed by dislocation creep. In Figure 3d, we illustrate that the transition from LTP to dislocation creep is followed by strong localization (indicated by a strong increase of viscous strain rate in the anomaly) which then causes a temperature surge.

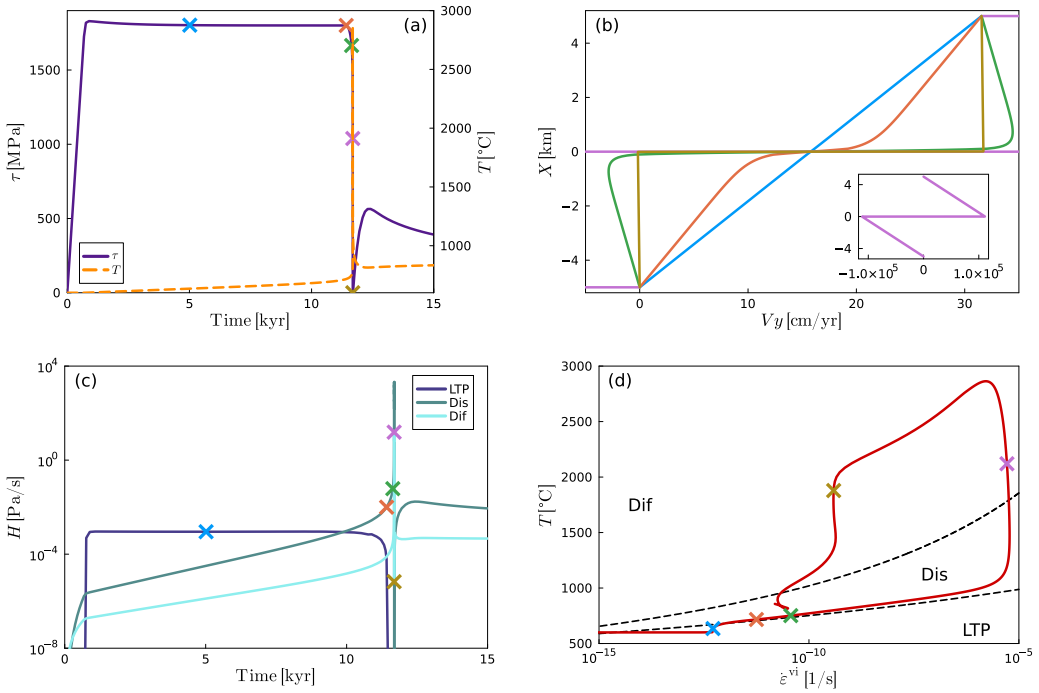

Figure 3. Representative model with thermal runaway. (a) Stress and maximum temperature evolution. Crosses denote time steps that are represented by lines in b and crosses in c,d. (b) Velocity profile during different stages of the model. Inset shows full range of the purple profile. Colors correspond to the time steps marked by crosses in a. (c) Dissipation of the three viscous deformation mechanisms. (d) Maximum temperature and maximum viscous strain rate evolution on deformation mechanism map from Figure 1b. Note that there are 5 kyr between blue and orange, but only a few seconds between purple and yellow.

3.2 Regularization

To investigate the effect of the viscosity regularization, we performed 50 simulations with identical material parameters but different spatial resolutions $dx_{\min}$ (minimum cell size: 0.125 - 2 m for a 10 km domain) and regularization viscosities η_{reg} (10^9 - 10^{18} Pa s). All simulations with $\eta_{\mathrm{reg}} < 10^{15}\,\mathrm{Pa\,s}$ exhibit the same stress evolution. For larger η_{reg}, localization is restricted by the regularization, resulting in a slower and incomplete stress release (Fig. 4a).

In Figure 4b, we show $\dot{\varepsilon}_{\mathrm{vi}}$-$T$-paths of experiments with different regularization viscosities. All models start in LTP, transition to dislocation creep and undergo an increase in viscous strain rate (localization) which is followed by heating (thermal runaway). Independently of η_{reg}, all simulations return to the same location in T-$\dot{\varepsilon}_{\mathrm{vi}}$-space after the runaway due to thermal diffusion. Colored dots indicate when each model starts to be affected by the regularization which prevents the effective viscosity to decrease and strain rate to increase further.

Maximum slip velocities ($V_{\max}$) are inversely correlated with η_{reg} and only become weakly resolution dependent at low η_{reg} (Fig. 4c). We observe a similar inverse correlation between η_{reg} and the maximum temperature ($T_{\max}$) which does however break at low η_{reg} (inset of Fig. 4c).

To quantify the width of the shear zone (d_{SZ}), we calculate the full-width-half-maximum (FWHM) of the strain rate peak when the model reaches its maximum velocity (see inset in Figure 4d). d_{SZ} decreases exponentially with decreasing η_{reg} and is independent of the spatial resolution until it reaches the size of a single cell (Fig. 4d).

Based on the results presented in this section, we choose a resolution equivalent to the orange lines in Figure 4c,d for the parameter study. This means that the size of the central quarter of the cells is a ten-thousandth of the domain size (e.g., 1 m for 10 km). In addition, we utilize $\eta_{\mathrm{reg}} = 10^{12}\,\mathrm{Pa\,s}$ to optimize performance while not significantly changing the mechanics of the problem.

3.3 Nondimensionalization

Thermal runaway occurs for a range of different material parameters and boundary conditions. We find some general trends like high background strain rate and large

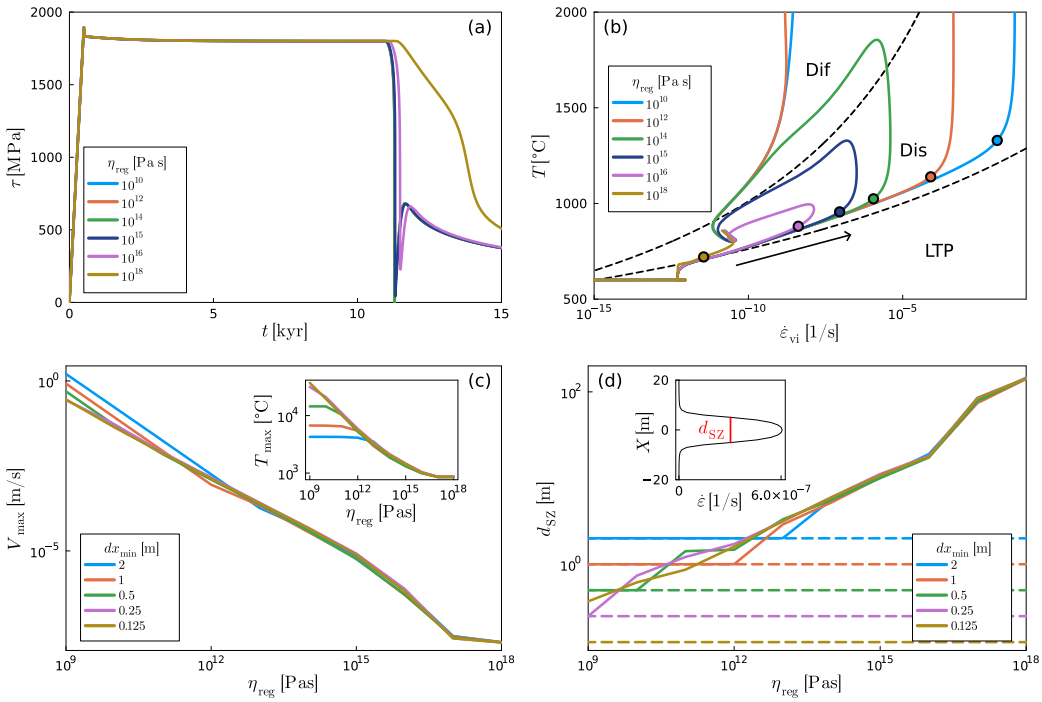

Figure 4. Effects of spatial resolution ($dx_{\min}$) and regularization viscosity (η_{reg}). (a) Temporal evolution of stress for different η_{reg}. Note that simulations with $\eta_{\mathrm{reg}} = 10^{10}$-$10^{15}$ Pa s all plot on top of another. (b) Temperature and viscous strain rate evolution in the center of the model for different η_{reg}. Black dashed lines and labels show the stability fields of the different deformation mechanisms (see Figure 1). Circles indicate when the respective experiments start to be affected by the regularization. Arrow indicates direction of temporal evolution. (c) Maximum slip velocity as function of resolution and η_{reg}. Inset shows maximum temperature. (d) Shear zone thickness (FWHM of strain rate anomaly, see inset) as function of resolution and η_{reg}. Dashed lines show the size of $dx_{\min}$.

model domains leading to thermal runaway more frequently (supplementary Figure S1) but no single parameter can yield a reliable prediction whether runaway occurs or not. To uncover the underlying mechanisms and identify the crucial scales that can predict the occurrence of thermal runaway, we nondimensionalize the energy conservation equation (eq. (4)). We define characteristic values for temperature (T_{c}), stress (τ_{c}), time (t_{c}) and length (l_{c}). Then, each dimensional quantity is replaced by the product of the appropriate characteristic value and the nondimensional quantity:

$$T = T_{\mathrm{c}}\, T', x = l_{\mathrm{c}}\, x', t = t_{\mathrm{c}}\, t', \tau = \tau_{\mathrm{c}}\, \tau', \tag{20}$$

where the subscript $_{\mathrm{c}}$ denotes each characteristic scale and $'$ denotes the nondimensionalized quantities. Applying this scaling to equation (4) yields:

$$\frac{\partial T'}{\partial t'} = t_{\mathrm{c}} \frac{\kappa}{l_{\mathrm{c}}^2} \frac{\partial^2 T'}{\partial x'^2} + \frac{t_{\mathrm{c}}}{T_{\mathrm{c}}} \frac{1}{\rho\, C_p} \tau_{\mathrm{c}} \tau'\, \dot{\varepsilon}_{\mathrm{vi}}, \tag{21}$$

where

$$\kappa = \frac{\lambda}{\rho\, C_p}. \tag{22}$$

Based on the observations in section 3.1, we make the following assumptions to define the characteristic scales for time, temperature, stress and length:

(i) The occurrence of thermal runaway is governed by the conditions when stress relaxation starts (black crosses in Figure 2).

(ii) Stress relaxation starts after the transition from elastic loading to dislocation creep or after the transition from low-temperature to dislocation creep.

(iii) There is no significant amount of temperature change during elastic loading.

(iv) Temperature change before stress relaxation is homogeneous in the model domain.

Following from these assumptions, we define the characteristic scales as follows:

$$l_{\mathrm{c}} = h, \tag{23}$$

$$T_{\mathrm{c}} = \max(T_0,\, T_{\mathrm{t}}), \tag{24}$$

$$\tau_{\mathrm{c}} = \min(\tau_{\mathrm{dis},0},\, \sigma_{\mathrm{b}}), \tag{25}$$

$$t_{\mathrm{c}} = \frac{\tau_{\mathrm{c}}\, \omega_0}{2\, \dot{\varepsilon}_{\mathrm{bg}}\, G}, \tag{26}$$

where

$$
\begin{aligned}
T_\mathrm{t} &= \frac{Q_\mathrm{dis}}{\ln\left(\dfrac{\sigma_\mathrm{b}^n\, f_\mathrm{an}\, \omega_0\, A_\mathrm{dis}}{\dot{\varepsilon}_\mathrm{bg}}\right)}, \\
\tau_{\mathrm{dis},0} &= \left(\frac{\dot{\varepsilon}_\mathrm{bg}}{f_\mathrm{an}\, \omega_0\, A_\mathrm{dis}} e^{\frac{Q_\mathrm{dis}}{T_0}}\right)^{\frac{1}{n}}, \\
Q_\mathrm{dis} &= \frac{E_\mathrm{dis}}{R}, \\
f_\mathrm{an} &= \frac{1}{\omega_0} + \frac{h}{2L}\sqrt{\frac{\pi}{\ln(2)}}\frac{\omega_0 - 1}{\omega_0}\mathrm{erf}\left(\frac{L}{h}\sqrt{\ln(2)}\right).
\end{aligned}
\tag{27}
$$

h is the full-width-half-maximum of the anomaly, T_0 the initial temperature, σ_b the back-stress of low-temperature plasticity, ω_0 the perturbation in the center of the anomaly, $\dot{\varepsilon}_\mathrm{bg}$ the background strain rate imposed by the boundary conditions, G the shear modulus and f_an describes the shape, size and strength of the anomaly. A detailed derivation is presented in the supplementary text S1. Equations (24) and (25) unite the scenarios that reach σ_LTP ($T_\mathrm{c} = T_\mathrm{t}$, $\tau_\mathrm{c} = \sigma_\mathrm{b}$, Figure 2a,c) with those that do not ($T_\mathrm{c} = T_0$, $\tau_\mathrm{c} = \tau_{\mathrm{dis},0}$, Figure 2b,d).

Substituting the characteristic scales l_c and t_c into equation (21) yields

$$
\frac{\partial T'}{\partial t'} = \underbrace{\frac{\tau_\mathrm{c}\,\omega_0}{2\,\dot{\varepsilon}_\mathrm{bg}\,G}}_{t_\mathrm{r}} \underbrace{\frac{\kappa}{h^2}}_{t_\mathrm{d}^{-1}} \frac{\partial^2 T'}{\partial x'^2} + \underbrace{\frac{1}{\rho\, C_p\, T_\mathrm{c}}}_{u_\mathrm{th}^{-1}} \underbrace{\frac{\tau_c^2}{2\,G\,f_\mathrm{an}}}_{u_\mathrm{el}} \omega(x)\, \tau'^{n+1}\, e^{\frac{Q_\mathrm{dis}}{T_\mathrm{c}}\frac{T'-1}{T'}}. \tag{28}
$$

where t_r is the stress relaxation time scale of the host rock, t_d is the thermal diffusion time scale of the anomaly, u_th the thermal energy density and u_el the stored elastic energy density (full derivation in supplementary text S1). For readability, we do not substitute in T_c and τ_c at this point.

3.4 Nondimensional regimes

The nondimensional analysis suggests that temperature evolution is characterized by two scales. (i) $t_\mathrm{r}/t_\mathrm{d}$, the ratio between the characteristic stress relaxation time and the characteristic heat diffusion time. (ii) $u_\mathrm{el}/u_\mathrm{th}$, the ratio between the characteristic, elastic energy density and the characteristic thermal energy density. This scale represents the conversion of elastic energy to thermal energy during the runaway (e.g., Ogawa, 1987; Kameyama et al., 1999; Regenauer-Lieb & Yuen, 2003). We observe that the entire model domain releases stress (i.e., elastic energy), but the majority of heating occurs in the anomaly. Therefore, we multiply u_el by the domain size L and u_th by the anomaly

size h to obtain absolute energies instead of energy densities. This yields the following 4 scales:

$$
\begin{aligned}
t_\mathrm{r} &= \frac{\tau_\mathrm{c}\,\omega_0}{2\,\dot{\varepsilon}_\mathrm{bg}\,G}, \\
t_\mathrm{d} &= \frac{h^2}{\kappa}, \\
U_\mathrm{el} &= u_\mathrm{el}\,L = \frac{\tau_\mathrm{c}^2\,L}{2\,G\,f_\mathrm{an}}, \\
U_\mathrm{th} &= u_\mathrm{th}\,h = \rho\,C_p\,T_\mathrm{c}\,h.
\end{aligned}
\tag{29}
$$

The occurrence of thermal runaway is accompanied by a spike in temperature and velocity, along with a rapid decrease in stress (Figure 3). To identify models with a temperature spike, we calculate ΔT_ex, the difference between the maximum temperature and the temperature at the end of the simulation. Plotting ΔT_ex against the ratios $t_\mathrm{r}/t_\mathrm{d}$ and $U_\mathrm{el}/U_\mathrm{th}$ reveals that all simulations with an ω_0 between 2 and 10 fall into two regimes with little overlap (Figure 5a). Maximum temperature rise, maximum temperature gradient, maximum stress gradient and maximum velocity increase all show near identical patterns (supplementary Figure S2).

If stress relaxation is fast compared to heat diffusion (low $t_\mathrm{r}/t_\mathrm{d}$) and the stored elastic energy is large compared to the thermal energy (high $U_\mathrm{el}/U_\mathrm{th}$), thermal runaway occurs. The regime boundary is well defined for $U_\mathrm{el}/U_\mathrm{th} > 0.5$, but changes slope for lower values. Runaway cases at $U_\mathrm{el}/U_\mathrm{th} < 0.5$ exhibit lower ΔT_ex, (i.e., less pronounced temperature peaks).

For $\omega_0 <= 1.1$ and $\omega_0 = 100$, we observe about 50 models that plot in the runaway field without showing the characteristics of thermal runaway (Figure 5b). The causes for these deviations are discussed in section 4.3.1.

4 Discussion

4.1 Regularization

The regularization viscosity in our rheological model inhibits localization to one cell which would lead to temperatures beyond 10'000 °C and viscosities < 1 Pa s. By providing a lower viscosity limit, the regularization facilitates numerical stability and results in shorter solution times.

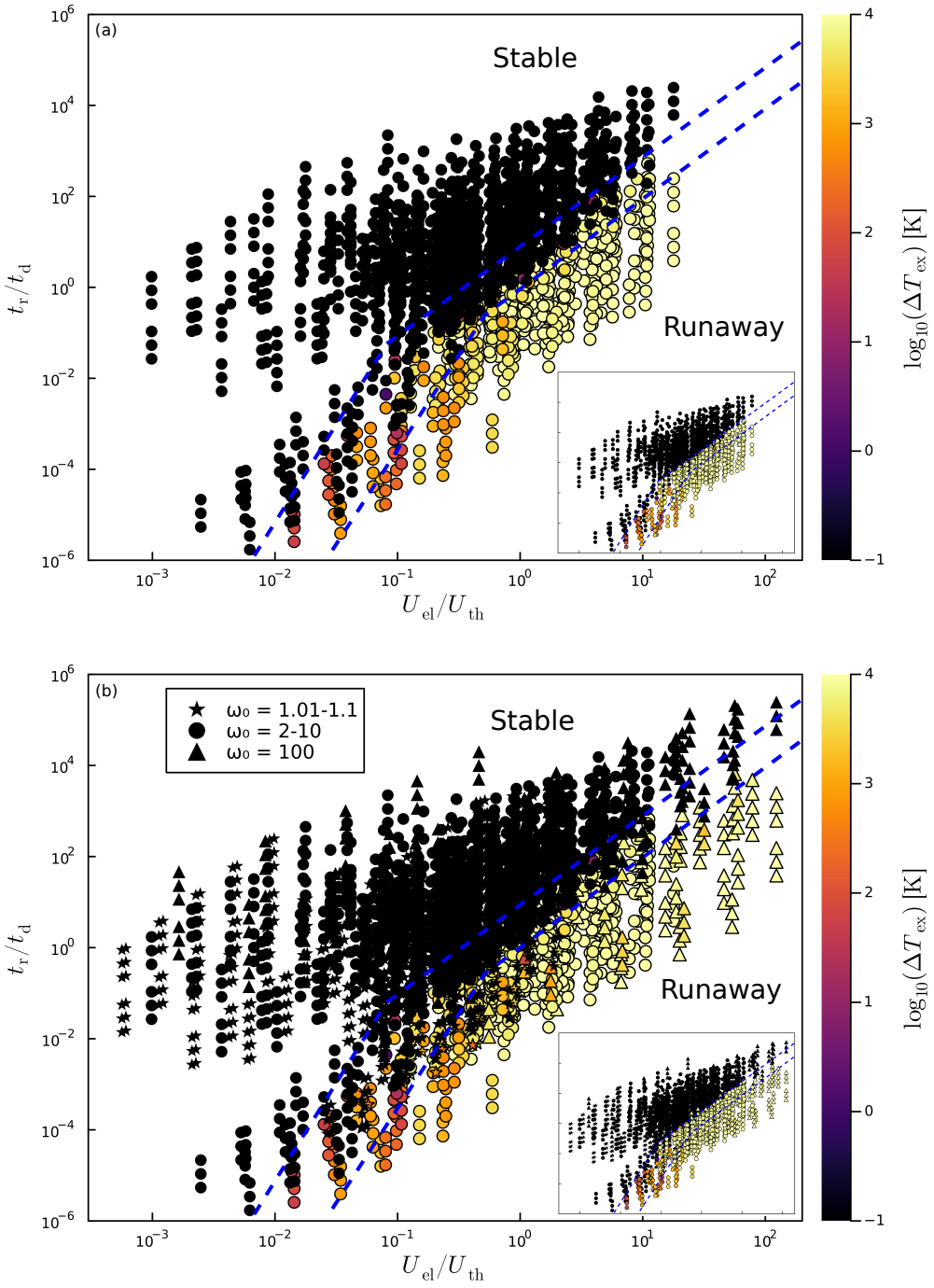

Figure 5. Maximum excess temperature rise ΔT_{ex} as a function of two non-dimensional parameters. t_r/t_d denotes the relation between the stress relaxation time scale and the heat diffusion time scale. U_{el}/U_{th} denotes the ratio between elastic and thermal energy at the start of stress relaxation. Area between dashed blue lines is the transition from the stable to the runaway regime. (a) Models with $\omega_0 = 2 - 10$. (b) All models. Insets show same plots but high ΔT_{ex} plot on top of low ΔT_{ex}. Note that the colorbar is truncated towards low values.

Furthermore, η_{reg} allows us to introduce a grid-independent length scale that controls the minimum width of the localized shear zone. As long as this length scale is larger than the maximum model resolution, shear zone width, maximum slip velocity and maximum temperature are all resolution-independent, showing exponential relationships with η_{reg} (Fig. 4).

Up to and including $\eta_{\mathrm{reg}} = 10^{15}\,\mathrm{Pa\,s}$, we observe no significant changes in the stress evolution of the models (Figure 4a). While this value is large in the context of our study, it is still well below the lower viscosity cut-off of geodynamic models which is commonly $10^{18}\,\mathrm{Pa\,s}$ or even higher (e.g., Thielmann & Kaus, 2012; Piccolo et al., 2019; Glerum et al., 2018). This implies that thermal runaway with temperature and velocity spikes, as described in section 3.1, is unlikely to be observable in large scale geodynamic models. Maximum temperature changes and heating rates in such studies are usually limited (e.g., Leloup et al., 1999; Hartz & Podladchikov, 2008; Thielmann & Kaus, 2012; Devès et al., 2014; Schmalholz & Duretz, 2015).

4.2 Low-temperature plasticity

Diffusion and dislocation creep flow laws for olivine predict viscosities greater than 10^{24} Pa s for the cores of subducting slabs (e.g., Karato et al., 2001; Billen, 2010; Li et al., 2019). Even for strain rates as low as $10^{-15}\,\mathrm{s}^{-1}$, these viscosities imply stresses of more than 2 GPa. As low-temperature plasticity limits stresses to less than 2 GPa, it plays a crucial role in such settings. Under loading, LTP causes stress to plateau for several thousand years before temperatures are high enough for dislocation creep to relax the stress and potentially trigger thermal runaway.

This has implications for studies that do not include LTP in their rheological model. Unless initial temperatures are high enough for other creep mechanisms to limit stresses to less than 2 GPa, the models will reach conditions that should be naturally inadmissible (e.g., Kameyama et al., 1999). This leads to much more violent runaway events as the released elastic energy is proportional to the square of the stress before release (eq. (28)). As an example, the parameter set used for Figure 4 with $\eta_{\mathrm{reg}} = 10^{12}\,\mathrm{Pa\,s}$ produces a maximum temperature of 144'000 °C when LTP is not considered compared to 5'500 °C with LTP.

The influence of LTP also complicates the definition of a critical stress that can trigger thermal runaway as presented by Braeck et al. (2009) because this critical stress might be unreachable due to low-temperature plasticity. Instead, LTP allows for models to significantly heat up at the LTP-limit and eventually enter thermal runaway at much lower stresses than would be predicted by a scaling law not considering LTP. Whether LTP helps or hinders thermal runaway is discussed in section 4.3.2.

4.3 Nondimensional scales

Elastic loading, heating at the LTP-limit, stress relaxation, thermal runaway, reloading and repeated relaxation are all transient processes that depend on the current conditions, opposed to the initial conditions and are therefore inherently difficult to predict. This problem gets amplified by nonlinear relationships such as composite rheologies that include dislocation creep and/or low-temperature plasticity. On top of that, heat diffusion causes time- and space-dependent temperature conditions while strain localization does the same to strain rate conditions and reduces the size the anomaly.

To approach this challenge, we decide to approximate the conditions at stress release by the transition from LTP-dominated to dislocation-dominated creep (eq. (24)-(26)). Furthermore, we assume that beyond these conditions, the system is entirely governed by dislocation creep and disregard diffusion creep. This allows us to identify two nondimensional numbers ($t_\mathrm{r}/t_\mathrm{d}$ and $U_\mathrm{el}/U_\mathrm{th}$) that can estimate the occurrence of thermal runaway based on the material's rheological and thermal properties, size of system and anomaly, as well as initial temperature and background strain rate.

$t_\mathrm{r}/t_\mathrm{d}$ describes the competition between heating by stress relaxation and cooling by diffusion, a concept already described by Gruntfest (1963) that reappears in different studies on ductile localization (e.g., Yuen et al., 1978; Ogawa, 1987; Kiss et al., 2019). $U_\mathrm{el}/U_\mathrm{th}$ is the ratio of elastic to thermal energy at stress release. The conversion of the former into the latter has been named as the driver of thermal runaway (e.g., Ogawa, 1987; Kameyama et al., 1999; Regenauer-Lieb & Yuen, 2003). Thermal runaway is facilitated by a low $t_\mathrm{r}/t_\mathrm{d}$ (i.e., stress release is faster than thermal diffusion) and a high $U_\mathrm{el}/U_\mathrm{th}$ (i.e., stress and deforming domain are large while temperature is low).

Despite the aforementioned transient processes and nonlinear relationships, these two ratios split all experiments with $2.0 <= \omega_0 <= 10$ into a stable and runaway regime

(Figure 5a). The regime boundary follows the relationship $t_r/t_d \propto (U_{el}/U_{th})^2$ for most models, but bends towards a minimum U_{el}/U_{th} of about 10^{-3}. This suggests that there is a minimum required energy ratio to cause thermal runaway. Braeck et al. (2009) observe a similarly shaped regime boundary for the initial stress which they term "critical stress".

4.3.1 Failed runaway

Figure 5b shows that about 5% of models with $\omega_0 <= 1.1$ or $\omega_0 = 100$ do not undergo thermal runaway despite falling in the runaway regime. The vast majority of these models have an $\omega_0 <= 1.1$ and share a common feature: As the difference between host rock and anomaly is very small, localization is slower than stress relaxation. This means that large portions of the stored elastic energy are converted to heat outside the anomaly, thus violating the assumptions that the scaling is based on. When these models localize, there is not enough elastic energy left to cause a temperature spike. Many of them still show a period of rapid stress drop and temperature rise towards the end of the relaxation (solid lines in Figure 6a,b), but they are much closer to what Braeck et al. (2009) termed "adiabatic runaway". If the scaling could account for the delayed, and therefore smaller, stress drop, these models would plot at lower U_{el}/U_{th} in the stable regime (Figure 5b).

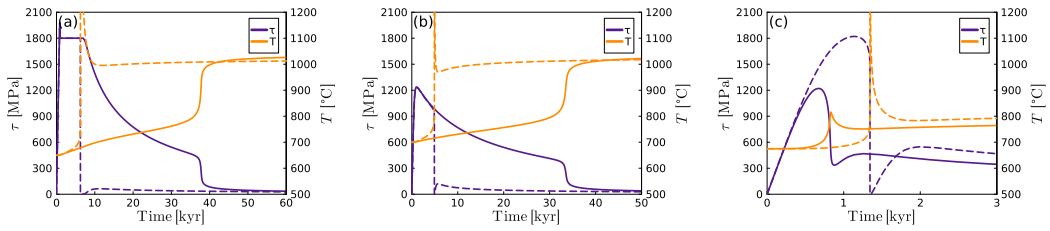

Figure 6. Failed runaways. Solid lines show stress and temperature evolution for representative models that did not experience thermal runaway but plot inside the runaway regime (Figure 5b). (a,b) $\omega_0 <= 1.1$ with delayed stress localization. Dashed lines show same parameter combinations with $\omega_0 = 2$ exhibiting thermal runaway. (c) $\omega_0 = 100$ with incomplete localization. Dashed lines show the same model with $\omega_0 = 10$ exhibiting thermal runaway.

For the few models with $\omega_0 = 100$ that do not undergo runaway despite falling in the runaway regime, we propose that the difference between host rock and anomaly

is too large for the models to exhibit progressive localization inside the anomaly. Consequently, heat is distributed in a larger area and the anomaly does not weaken enough to result in thermal runaway. 5 out of 7 of these models result in thermal runaway for a lower values of ω_0 (dashed lines in Figure 6c). The fact that some settings are more likely to result in thermal runaway by increasing ω_0 (Figure 6a,b) and others by decreasing ω_0 (Figure 6c) demonstrates the complex transient interactions that are difficult to fully capture in a scaling.

4.3.2 Comparison to previous studies

In this study, we propose that thermal runaway is governed by the ratios $t_\mathrm{r}/t_\mathrm{d}$ and $U_\mathrm{el}/U_\mathrm{th}$. Similar nondimensional scalings have been proposed in previous studies. Ogawa (1987) presents three scales, the Gruntfest number (Gruntfest, 1963), similar to the inverse of $t_\mathrm{r}/t_\mathrm{d}$, a ratio of elastic to ductile stiffness which bears similarities with the inverse of $U_\mathrm{el}/U_\mathrm{th}$ and a quantity characterizing the anomaly strength and size. Braeck et al. (2009) include the anomaly description into the other two scales to reduce the problem to two ratios. The first of which is almost identical to $t_\mathrm{r}/t_\mathrm{d}$ whereas the second one relates the boundary stress to a critical stress derived from an analytical solution. Furthermore, our characterization of the anomaly (f_an) is similar to the one used by Braeck et al. (2009). Both of the previous studies describe a rheology consisting of elasticity and dislocation creep, neglecting the stress-limiting effect of LTP which is included in equation (28) and the potential interference of diffusion creep. On top of that, the study of Braeck et al. (2009) applies stress boundary conditions which exclude the transient effects that occur during loading and low-temperature plasticity.

The nondimensional scaling also agrees with previous studies which show that higher background strain rates (lower $t_\mathrm{r}/t_\mathrm{d}$) facilitate thermal runaway while higher initial temperatures (larger $U_\mathrm{el}/U_\mathrm{th}$) hamper it (Kameyama et al., 1999; Kaus & Podladchikov, 2006; Thielmann, 2018).

Kameyama et al. (1999) concluded that LTP inhibits thermal runaway for constant strain rate boundary conditions by lowering the maximum stress and thereby the amount of viscous dissipation. Given the quadratic dependence of $U_\mathrm{el}/U_\mathrm{th}$ on maximum shear stress (eq. (29)), LTP does in fact have a negative effect on thermal runaway probability at low temperatures. It does, however, not inhibit it (Figures 2-4), and often just de-

lays the runaway. The reason LTP inhibited runaway in Kameyama et al. (1999) is the use of a thermal anomaly which diffuses away during the delay caused by LTP.

4.4 Design choices and limitations

Numerical models inherently involve some artificial components like the initial anomaly (Figure 1a). The majority of previous studies chose a temperature perturbation (Yuen et al., 1978; Ogawa, 1987; Kameyama et al., 1999; Kaus & Podladchikov, 2006; Braeck et al., 2009; Kiss et al., 2019) whereas we use a rheological perturbation, similar to Thielmann et al. (2015). Such a local change in material property is consistent with a heterogeneity in composition or water content and has the advantage of being independent of time (John et al., 2009). Thermal anomalies diffuse over time and smear out for low strain rates (e.g., Kameyama et al., 1999) and small anomalies (e.g., Ogawa, 1987).

Another arbitrary choice is the shape of the perturbation. The majority of previous studies used a step-like perturbation with a sharp boundary and constant value wheres Yuen et al. (1978) employed a Gaussian-like perturbation. We tested both and observed that the Gaussian perturbation facilitates localization for large anomalies. In 131 cases, a step-like anomaly did not result in runaway and a Gaussian anomaly did (supplementary Figure S3). There is also a very small number of cases (less than 10 out of 6000), where the step-like anomaly resulted in runaway and the Gaussian perturbation did not.

Our rheological model does not account for the possibility of brittle failure and the ultimate strength of the crystal lattice. The Drucker-Prager yield criterion (Drucker & Prager, 1952) predicts a yield strength of 5 GPa for a pressure of 10 GPa (Table 1) and a typical friction angle of 30°. The theoretical strength of atomic bonds is on the order 10 % of the shear modulus (Renshaw & Schulson, 2007) which equates to 4 - 16 GPa for our parameter range. With LTP, such stresses are unreachable.

We neglect the inertial terms from equation (3) as they do not influence the occurrence of thermal runaway but only become important at the late stages of the runaway which are not the focus of our study.

Adding grain size evolution to our rheological model or using a smaller initial grain size would likely result in lower characteristic stresses. Given the quadratic dependence of $U_{\mathrm{el}}/U_{\mathrm{th}}$ compared to the linear dependence of $t_{\mathrm{r}}/t_{\mathrm{d}}$ on τ_{c}, this would reduce the like-

lihood of thermal runaway. Thielmann (2018) shows a similar result where reduced initial grain size shifts the regime boundary towards lower temperatures and in a viscous lithosphere study, Foley (2018) concludes that grain size evolution limits temperature growth due to shear heating. However, Cross and Skemer (2019) suggest that dynamic recrystallization (i.e., grain size reduction) is strain dependent and that only about 10% of olivine grains recrystallize at a strain of 1 for olivine. Since our models all release their stress before reaching a strain of 1 (many at less than 0.1), we would not expect a significant amount of grain size reduction that could influence the thermal runaway.

4.5 Implications for deep earthquakes

Intermediate- and deep-focus earthquakes are commonly associated with the cold cores of subducting slabs (Houston, 2015; Zhan, 2020) which can reach depths of 500 km with temperatures ranging from 500 °C (Tonga) to 800 °C (Bolivia) (e.g., Gasc et al., 2022). Our models demonstrate that thermal runaway can occur at such conditions, even at lower strain rates than assumed by Gasc et al. (2022). Maximum slip velocities and strain rates reach the values associated with pseudotachylyte formation ($v \approx 1\,\mathrm{m\,s^{-1}}$, $\dot{\varepsilon} \approx 1\,\mathrm{s^{-1}}$; Spray, 1995; Del Gaudio et al., 2009) which are commonly interpreted as the products of deep earthquakes (e.g., Andersen et al., 2008).

We observe thermal runaway with rheological perturbations as low as 1% ($\omega_0 = 1.01$) which suggests that natural heterogeneities in composition, water content or isotropy could all be sufficient triggers for deep earthquakes. The quadratic, inverse dependence of $t_\mathrm{r}/t_\mathrm{d}$ on the perturbation size h does however demonstrate that thermal runaway is unlikely to initiate at the mm-scale. This indicates that thermal runaway could be the second phase of a dual-mechanism process which is initiated by dehydration embrittlement (intermediate-depth) or transformational faulting (deep-focus) (McGuire et al., 1997; Bezada & Humphreys, 2012; Zhan, 2020). One could also imagine a scenario where large scale shear heating causes a moderate temperature rise which triggers transformational faulting which then seeds localized thermal runaway.

5 Conclusions

In this study, we present thermomechanical 1D models of velocity-driven simple-shear deformation with a visco-elastic rheology comprising diffusion creep, dislocation

creep and low-temperature plasticity. The rheological model is augmented by a regularization viscosity that provides stability during strain localization and removes resolution dependencies. Low-temperature plasticity plays a critical role in this system, limiting deviatoric stresses and thereby delaying thermal runaway by up to thousands of years.

We observe shear zone formation accompanied by a moderate (100 - 300 K) temperature increase or thermal runaway accompanied by strong localization and a temperature surge of thousands of Kelvin. We derive two nondimensional ratios that combine initial conditions and material parameters and allow us to estimate the occurrence of thermal runaway. $t_\mathrm{r}/t_\mathrm{d}$ describes the competition of heat generation from stress relaxation and heat loss due to thermal diffusion whereas $U_\mathrm{el}/U_\mathrm{th}$ compares the stored elastic energy to thermal energy in the system. Thermal runaway occurs if $t_\mathrm{r}/t_\mathrm{d}$ is small and $U_\mathrm{el}/U_\mathrm{th}$ is large.

Our numerical experiments demonstrate that thermal runaway is a viable mechanism to cause fast slip events that are in line with intermediate- and deep-focus earthquakes, as well as pseudotachylyte formation at conditions comparable to cores of subducting slabs.

Acknowledgments

A.S. and M.T. were funded by the DFG grant TH 2076/8-1 awarded to M.T.. D.K. acknowledges the European Research Council (Consolidator Grant 771143 (MAGMA) awarded to Boris J.P. Kaus), and the Research Council of Norway and the industry partners of NCS2030 (RCN project number 331644) for their support.

Open Research Section

Software for this research is available on zenodo at https://doi.org/10.5281/zenodo.10200918.

References

Andersen, T. B., Mair, K., Austrheim, H., Podladchikov, Y. Y., & Vrijmoed, J. C. (2008). Stress release in exhumed intermediate and deep earthquakes determined from ultramafic pseudotachylyte. *Geology*, *36*(12), 995–998.

Austin, N., Evans, B., Herwegh, M., & Ebert, A. (2008). Strain localization in the Morcles nappe (Helvetic Alps, switzerland). *swiss Journal of Geosciences*, *101*, 341–360.

Bezada, M., & Humphreys, E. (2012). Contrasting rupture processes during the April 11, 2010 deep-focus earthquake beneath Granada, Spain. *Earth and Planetary Science Letters*, *353*, 38–46.

Billen, M. I. (2010). Slab dynamics in the transition zone. *Physics of the Earth and planetary interiors*, *183*(1-2), 296–308.

Braeck, S., Podladchikov, Y. Y., & Medvedev, S. (2009). Spontaneous dissipation of elastic energy by self-localizing thermal runaway. *Physical Review E*, *80*(4), 046105.

Braun, J., Chéry, J., Poliakov, A., Mainprice, D., Vauchez, A., Tomassi, A., & Daignières, M. (1999). A simple parameterization of strain localization in the ductile regime due to grain size reduction: A case study for olivine. *Journal of Geophysical Research: Solid Earth*, *104*(B11), 25167–25181.

Brinkman, H. (1951). Heat effects in capillary flow i. *Applied Scientific Research*, *2*, 120–124.

Byerlee, J. (1978). Friction of rocks. In *Rock friction and earthquake prediction* (pp. 615–626). Birkhäuser, Basel.

Chrysochoos, A., & Belmahjoub, F. (1992). Thermographic analysis of thermomechanical couplings. *Archives of Mechanics*, *44*(1), 55–68.

Cross, A., & Skemer, P. (2019). Rates of dynamic recrystallization in geologic materials. *Journal of Geophysical Research: Solid Earth*, *124*(2), 1324–1342.

De Borst, R., Sluys, L. J., Muhlhaus, H.-B., & Pamin, J. (1993). Fundamental issues in finite element analyses of localization of deformation. *Engineering computations*, *10*(2), 99–121.

Del Gaudio, P., Di Toro, G., Han, R., Hirose, T., Nielsen, S., Shimamoto, T., & Cavallo, A. (2009). Frictional melting of peridotite and seismic slip. *Journal of Geophysical Research: Solid Earth*, *114*(B6).

Devès, M. H., Tait, S. R., King, G. C., & Grandin, R. (2014). Strain heating in process zones; implications for metamorphism and partial melting in the lithosphere. *Earth and Planetary Science Letters*, *394*, 216–228.

Drucker, D. C., & Prager, W. (1952). Soil mechanics and plastic analysis or limit design. *Quarterly of applied mathematics*, *10*(2), 157–165.

Duretz, T., de Borst, R., Yamato, P., & Le Pourhiet, L. (2020). Toward robust and predictive geodynamic modeling: The way forward in frictional plasticity. *Geo-*

physical Research Letters, *47*(5), e2019GL086027.

Duretz, T., Räss, L., Podladchikov, Y., & Schmalholz, S. (2019). Resolving thermomechanical coupling in two and three dimensions: spontaneous strain localization owing to shear heating. *Geophysical Journal International*, *216*(1), 365–379.

Duretz, T., Schmalholz, S., Podladchikov, Y., & Yuen, D. (2014). Physics-controlled thickness of shear zones caused by viscous heating: Implications for crustal shear localization. *Geophysical Research Letters*, *41*(14), 4904–4911.

Foley, B. J. (2018). On the dynamics of coupled grain size evolution and shear heating in lithospheric shear zones. *Physics of the Earth and Planetary Interiors*, *283*, 7–25.

Frankel, S. P. (1950). Convergence rates of iterative treatments of partial differential equations. *Mathematics of Computation*, *4*(30), 65–75.

Gasc, J., Daigre, C., Moarefvand, A., Deldicque, D., Fauconnier, J., Gardonio, B., ... Schubnel, A. (2022). Deep-focus earthquakes: From high-temperature experiments to cold slabs. *Geology*, *50*(9), 1018–1022.

Gerya, T. V., & Yuen, D. A. (2003). Characteristics-based marker-in-cell method with conservative finite-differences schemes for modeling geological flows with strongly variable transport properties. *Physics of the Earth and Planetary Interiors*, *140*(4), 293–318.

Glerum, A., Thieulot, C., Fraters, M., Blom, C., & Spakman, W. (2018). Nonlinear viscoplasticity in aspect: benchmarking and applications to subduction. *Solid Earth*, *9*(2), 267–294.

Gruntfest, I. (1963). Thermal feedback in liquid flow; plane shear at constant stress. *Transactions of the Society of Rheology*, *7*(1), 195–207.

Hansen, L. N., Kumamoto, K. M., Thom, C. A., Wallis, D., Durham, W. B., Goldsby, D. L., ... Kohlstedt, D. L. (2019). Low-temperature plasticity in olivine: Grain size, strain hardening, and the strength of the lithosphere. *Journal of Geophysical Research: Solid Earth*, *124*(6), 5427–5449.

Hartz, E. H., & Podladchikov, Y. Y. (2008). Toasting the jelly sandwich: The effect of shear heating on lithospheric geotherms and strength. *Geology*, *36*(4), 331–334.

Hirth, G., & Kohlstedt, D. L. (2003). Rheology of the upper mantle and the man-

tle wedge: A view from the experimentalists. *Geophysical monograph-american geophysical union*, *138*, 83–106.

Hobbs, B., Ord, A., & Teyssier, C. (1986). Earthquakes in the ductile regime? *Pure and Applied Geophysics*, *124*, 309–336.

Holtzman, B., Chrysochoos, A., & Daridon, L. (2018). A thermomechanical framework for analysis of microstructural evolution: Application to olivine rocks at high temperature. *Journal of Geophysical Research: Solid Earth*, *123*(10), 8474–8507.

Houston, H. (2015). Deep earthquakes. In *Treatise on geophysics.* Elsevier.

Iordache, M.-M., & Willam, K. (1998). Localized failure analysis in elastoplastic Cosserat continua. *Computer Methods in Applied Mechanics and Engineering*, *151*(3-4), 559–586.

Jacquey, A. B., & Cacace, M. (2020). Multiphysics modeling of a brittle-ductile lithosphere: 1. Explicit visco-elasto-plastic formulation and its numerical implementation. *Journal of Geophysical Research: Solid Earth*, *125*(1), e2019JB018474.

Jacquey, A. B., Rattez, H., & Veveakis, M. (2021). Strain localization regularization and patterns formation in rate-dependent plastic materials with multiphysics coupling. *Journal of the Mechanics and Physics of Solids*, *152*, 104422.

John, T., Medvedev, S., Rüpke, L. H., Andersen, T. B., Podladchikov, Y. Y., & Austrheim, H. (2009). Generation of intermediate-depth earthquakes by self-localizing thermal runaway. *Nature Geoscience*, *2*(2), 137–140.

Kameyama, M., Yuen, D. A., & Fujimoto, H. (1997). The interaction of viscous heating with grain-size dependent rheology in the formation of localized slip zones. *Geophysical Research Letters*, *24*(20), 2523–2526.

Kameyama, M., Yuen, D. A., & Karato, S.-I. (1999). Thermal-mechanical effects of low-temperature plasticity (the Peierls mechanism) on the deformation of a viscoelastic shear zone. *Earth and Planetary Science Letters*, *168*(1-2), 159–172.

Karato, S.-i., Riedel, M. R., & Yuen, D. A. (2001). Rheological structure and deformation of subducted slabs in the mantle transition zone: implications for mantle circulation and deep earthquakes. *Physics of the Earth and Planetary Interiors*, *127*(1-4), 83–108.

Kaus, B. J. P., de Montserrat, A., Medinger, N., Riel, N., Cosarinky, M., Berlie, N., ... Duretz, T. (2023). *JuliaGeodynamics/GeoParams.jl: v0.5.1.* Zenodo. Retrieved from `https://doi.org/10.5281/zenodo.10050339`

Kaus, B. J. P., & Podladchikov, Y. Y. (2006). Initiation of localized shear zones in viscoelastoplastic rocks. *Journal of Geophysical Research: Solid Earth*, *111*(B4).

Kiss, D., Moulas, E., Kaus, B. J. P., & Spang, A. (2023). Decompression and fracturing caused by magmatically induced thermal stresses. *Journal of Geophysical Research: Solid Earth*, *128*(3), e2022JB025341.

Kiss, D., Podladchikov, Y. Y., Duretz, T., & Schmalholz, S. M. (2019). Spontaneous generation of ductile shear zones by thermal softening: Localization criterion, 1D to 3D modelling and application to the lithosphere. *Earth and planetary science letters*, *519*, 284–296.

Leloup, P. H., Ricard, Y., Battaglia, J., & Lacassin, R. (1999). Shear heating in continental strike-slip shear zones: model and field examples. *Geophysical Journal International*, *136*(1), 19–40.

Li, Z.-H., Gerya, T., & Connolly, J. A. (2019). Variability of subducting slab morphologies in the mantle transition zone: Insight from petrological-thermomechanical modeling. *Earth-Science Reviews*, *196*, 102874.

McGuire, J. J., Wiens, D. A., Shore, P. J., & Bevis, M. G. (1997). The March 9, 1994 (M w 7.6), deep Tonga earthquake: Rupture outside the seismically active slab. *Journal of Geophysical Research: Solid Earth*, *102*(B7), 15163–15182.

Mulyukova, E., & Bercovici, D. (2017). Formation of lithospheric shear zones: Effect of temperature on two-phase grain damage. *Physics of the Earth and Planetary Interiors*, *270*, 195–212.

Ogawa, M. (1987). Shear instability in a viscoelastic material as the cause of deep focus earthquakes. *Journal of Geophysical Research: Solid Earth*, *92*(B13), 13801–13810.

Piccolo, A., Palin, R. M., Kaus, B. J. P., & White, R. W. (2019). Generation of Earth's early continents from a relatively cool Archean mantle. *Geochemistry, Geophysics, Geosystems*, *20*(4), 1679–1697.

Räss, L., Utkin, I., Duretz, T., Omlin, S., & Podladchikov, Y. Y. (2022). Assess-

ing the robustness and scalability of the accelerated pseudo-transient method. *Geoscientific Model Development*, *15*(14), 5757–5786.

Regenauer-Lieb, K., & Yuen, D. (2003). Modeling shear zones in geological and planetary sciences: solid-and fluid-thermal–mechanical approaches. *Earth-Science Reviews*, *63*(3-4), 295–349.

Regenauer-Lieb, K., & Yuen, D. (2004). Positive feedback of interacting ductile faults from coupling of equation of state, rheology and thermal-mechanics. *Physics of the Earth and Planetary Interiors*, *142*(1-2), 113–135.

Regenauer-Lieb, K., & Yuen, D. A. (1998). Rapid conversion of elastic energy into plastic shear heating during incipient necking of the lithosphere. *Geophysical Research Letters*, *25*(14), 2737–2740.

Renshaw, C. E., & Schulson, E. M. (2007). Limits on rock strength under high confinement. *Earth and Planetary Science Letters*, *258*(1-2), 307–314.

Ricard, Y., & Bercovici, D. (2009). A continuum theory of grain size evolution and damage. *Journal of Geophysical Research: Solid Earth*, *114*(B1).

Rozel, A., Ricard, Y., & Bercovici, D. (2011). A thermodynamically self-consistent damage equation for grain size evolution during dynamic recrystallization. *Geophysical Journal International*, *184*(2), 719–728.

Ruh, J. B., Tokle, L., & Behr, W. M. (2022). Grain-size-evolution controls on lithospheric weakening during continental rifting. *Nature Geoscience*, *15*(7), 585–590.

Schmalholz, S., & Duretz, T. (2015). Shear zone and nappe formation by thermal softening, related stress and temperature evolution, and application to the Alps. *Journal of Metamorphic Geology*, *33*(8), 887–908.

Spray, J. G. (1995). Pseudotachylyte controversy: Fact or friction? *Geology*, *23*(12), 1119–1122.

Thielmann, M. (2018). Grain size assisted thermal runaway as a nucleation mechanism for continental mantle earthquakes: Impact of complex rheologies. *Tectonophysics*, *746*, 611–623.

Thielmann, M., & Kaus, B. J. (2012). Shear heating induced lithospheric-scale localization: Does it result in subduction? *Earth and Planetary Science Letters*, *359*, 1–13.

Thielmann, M., Rozel, A., Kaus, B. J. P., & Ricard, Y. (2015). Intermediate-depth

earthquake generation and shear zone formation caused by grain size reduction and shear heating. *Geology*, *43*(9), 791–794.

Yuen, D. A., Fleitout, L., Schubert, G., & Froidevaux, C. (1978). Shear deformation zones along major transform faults and subducting slabs. *Geophysical Journal International*, *54*(1), 93–119.

Zhan, Z. (2020). Mechanisms and implications of deep earthquakes. *Annual Review of Earth and Planetary Sciences*, *48*, 147–174.

Figure_1.

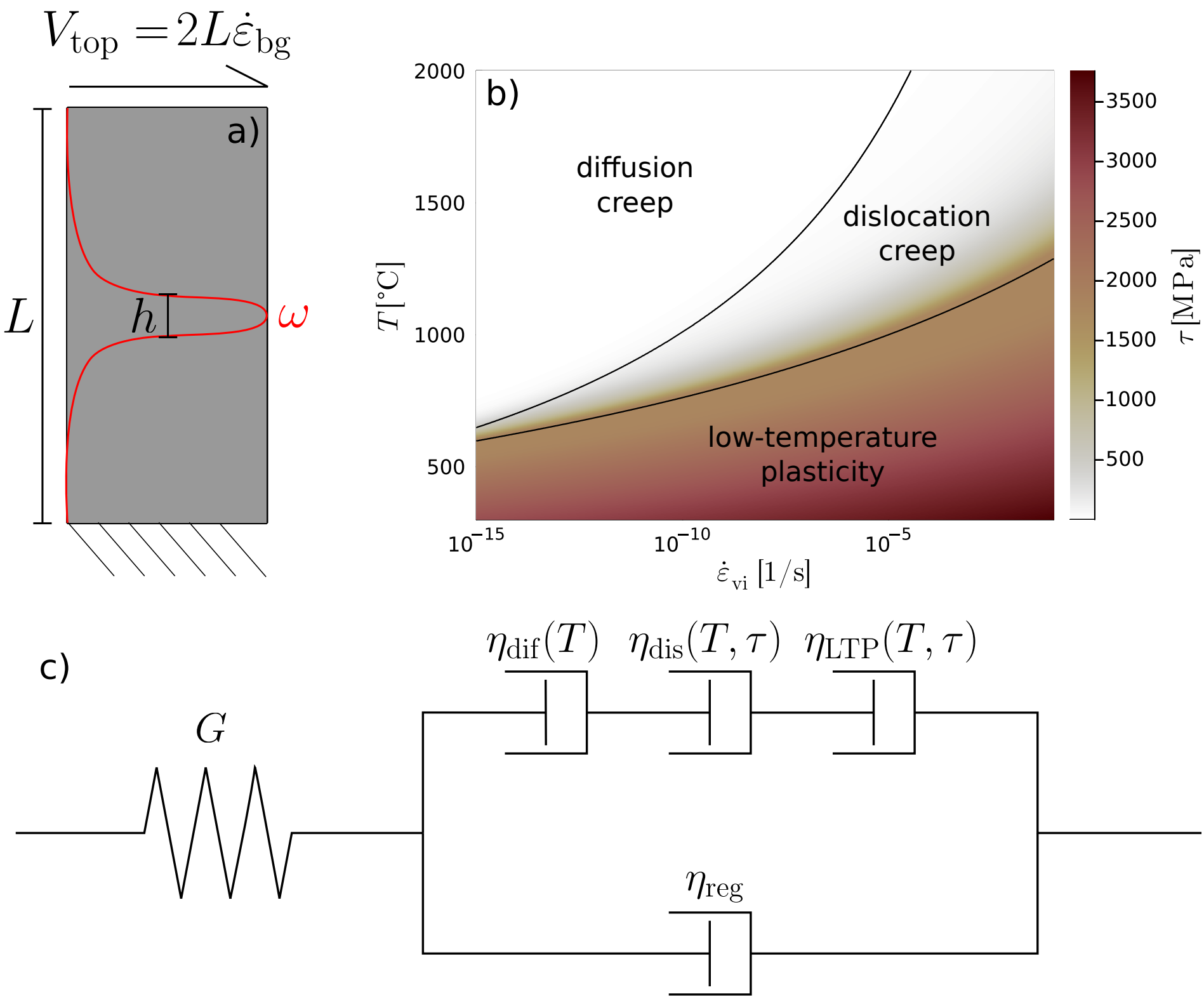
$V_{\mathrm{top}} = 2L\dot{\varepsilon}_{\mathrm{bg}}$
a)
L
h
ω
b)
diffusion creep
dislocation creep
low-temperature plasticity
$T\,[^{\circ}\mathrm{C}]$
2000
1500
1000
500
10^{-15}
10^{-10}
10^{-5}
$\dot{\varepsilon}_{\mathrm{vi}}\,[1/\mathrm{s}]$
3500
3000
2500
2000
1500
1000
500
$\tau\,[\mathrm{MPa}]$
c)
G
$\eta_{\mathrm{dif}}(T)$
$\eta_{\mathrm{dis}}(T,\tau)$
$\eta_{\mathrm{LTP}}(T,\tau)$
η_{reg}

Figure_2.

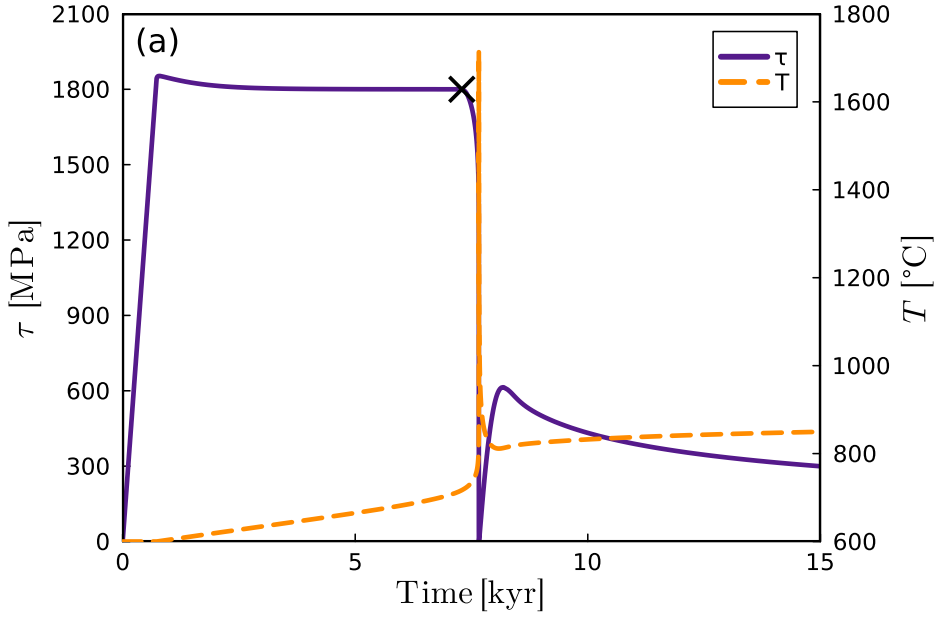
(a)
τ
T
τ [MPa]
T [°C]
Time [kyr]
0
300
600
900
1200
1500
1800
2100
600
800
1000
1200
1400
1600
1800
0
5
10
15

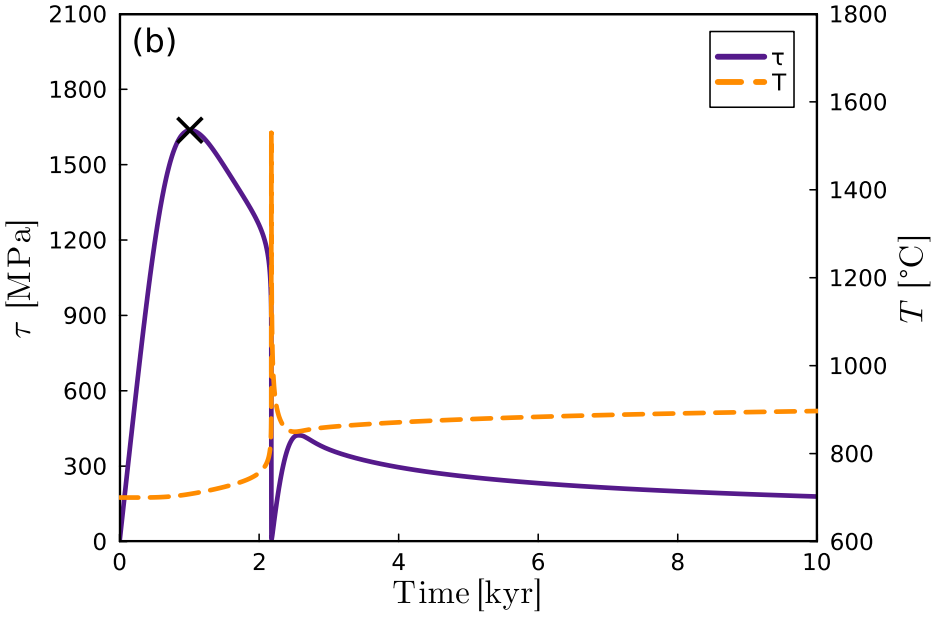
(b)
τ
T
τ [MPa]
T [°C]
Time [kyr]
0
300
600
900
1200
1500
1800
2100
600
800
1000
1200
1400
1600
1800
0
2
4
6
8
10

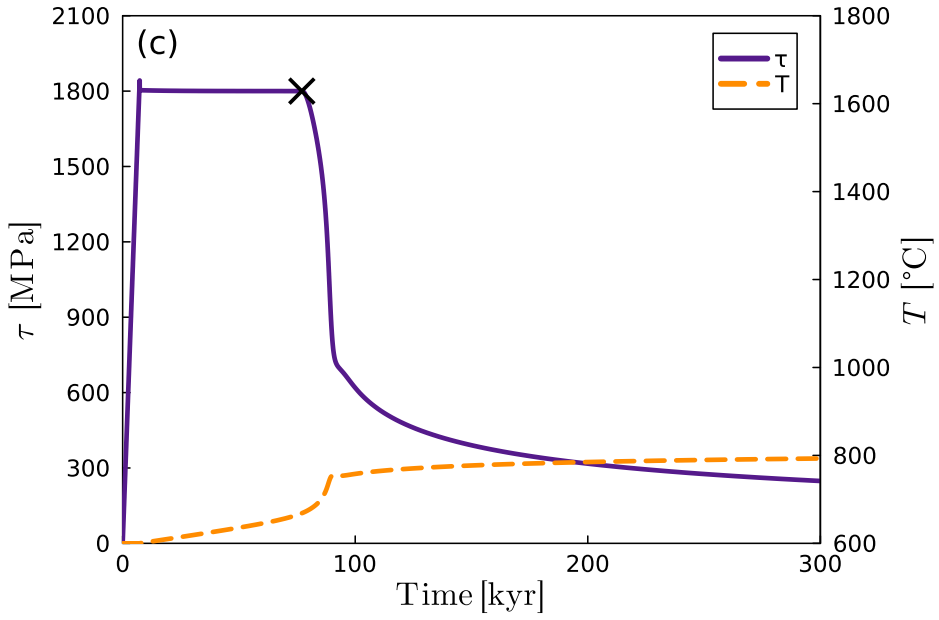
(c)
τ
T
τ [MPa]
T [°C]
Time [kyr]
0
300
600
900
1200
1500
1800
2100
600
800
1000
1200
1400
1600
1800
0
100
200
300

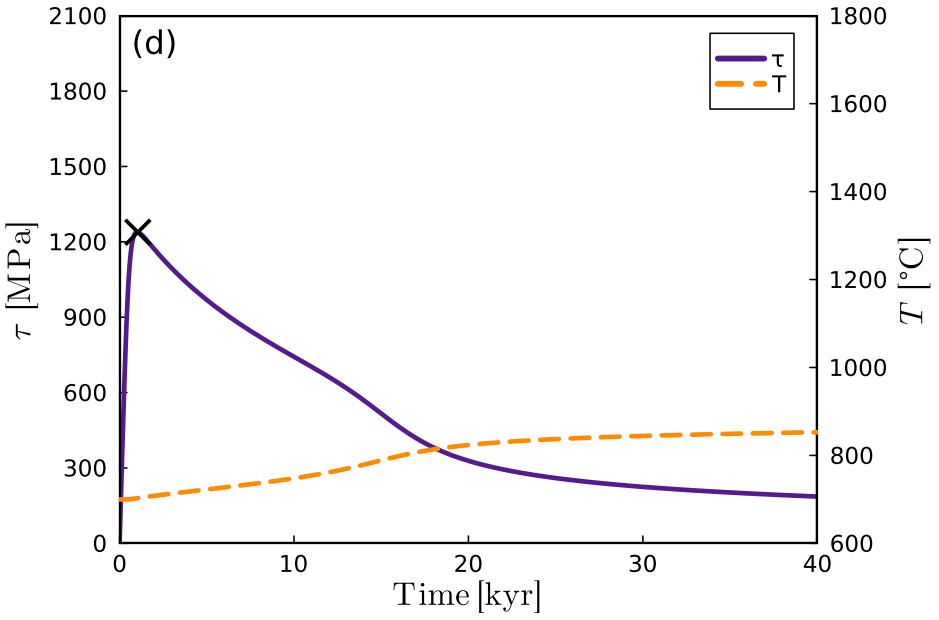
(d)
τ
T
τ [MPa]
T [°C]
Time [kyr]
0
300
600
900
1200
1500
1800
2100
600
800
1000
1200
1400
1600
1800
0
10
20
30
40

Figure_3.

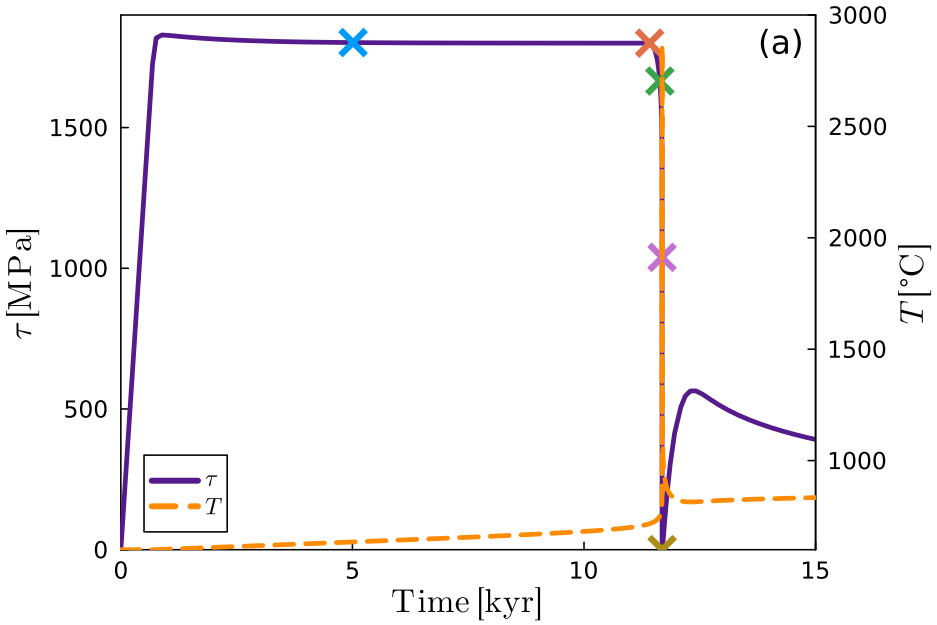
(a)
τ [MPa]
T [°C]
Time [kyr]
τ
T

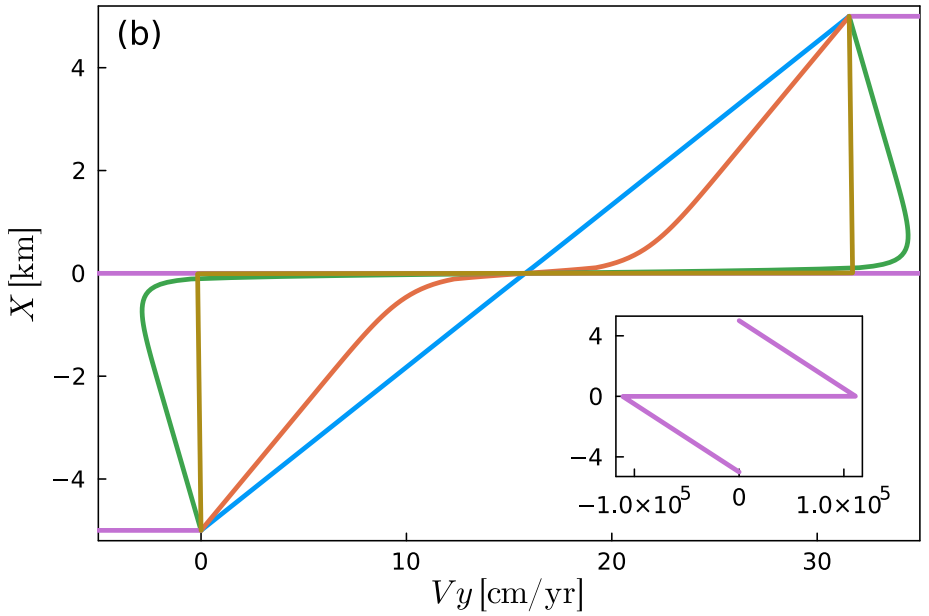
(b)
X [km]
Vy [cm/yr]

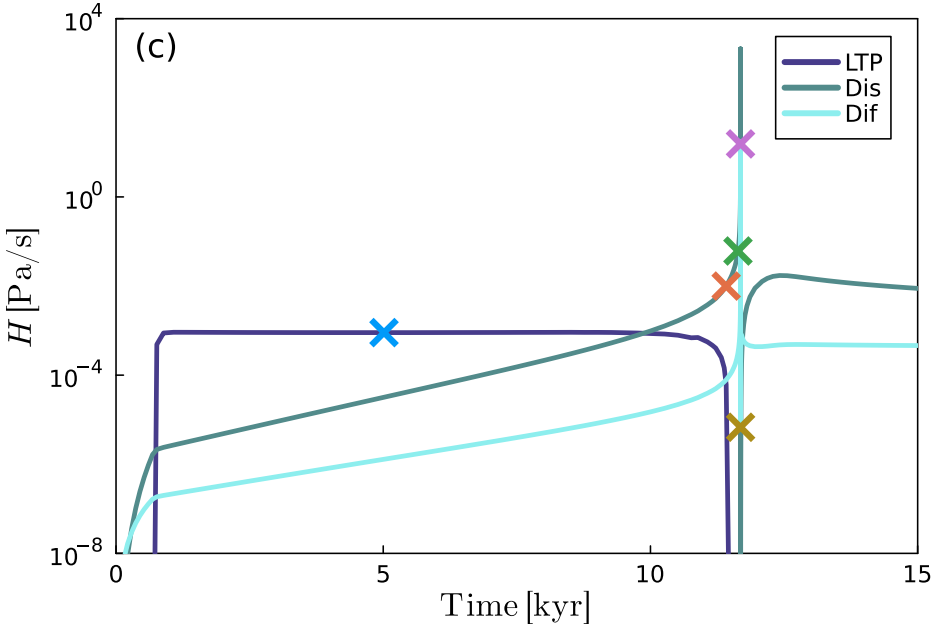
(c)
H [Pa/s]
Time [kyr]
LTP
Dis
Dif

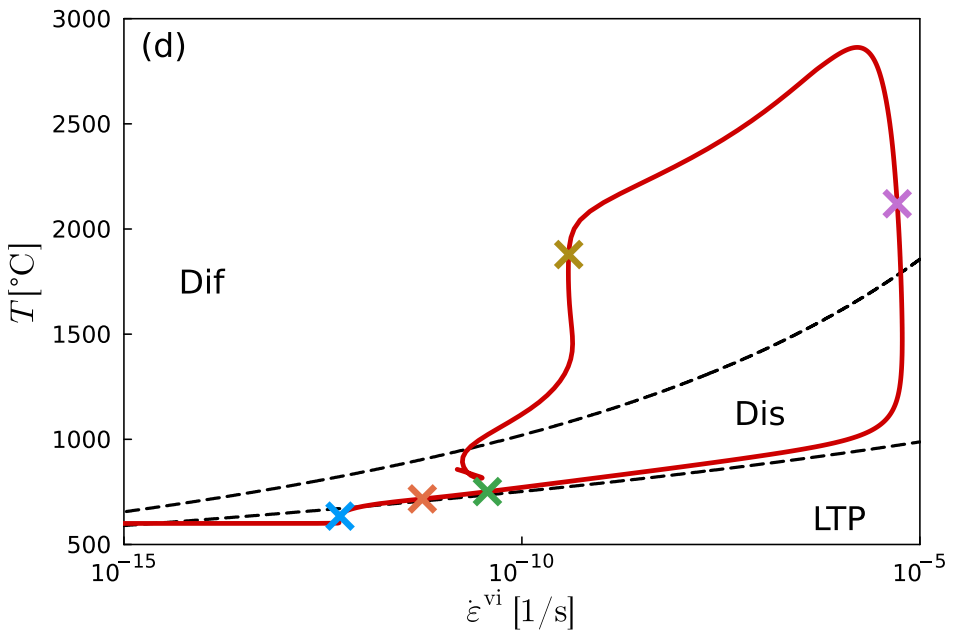
(d)
T [°C]
$\dot{\varepsilon}^{\mathrm{vi}}$ [1/s]
Dif
Dis
LTP

Figure_4.

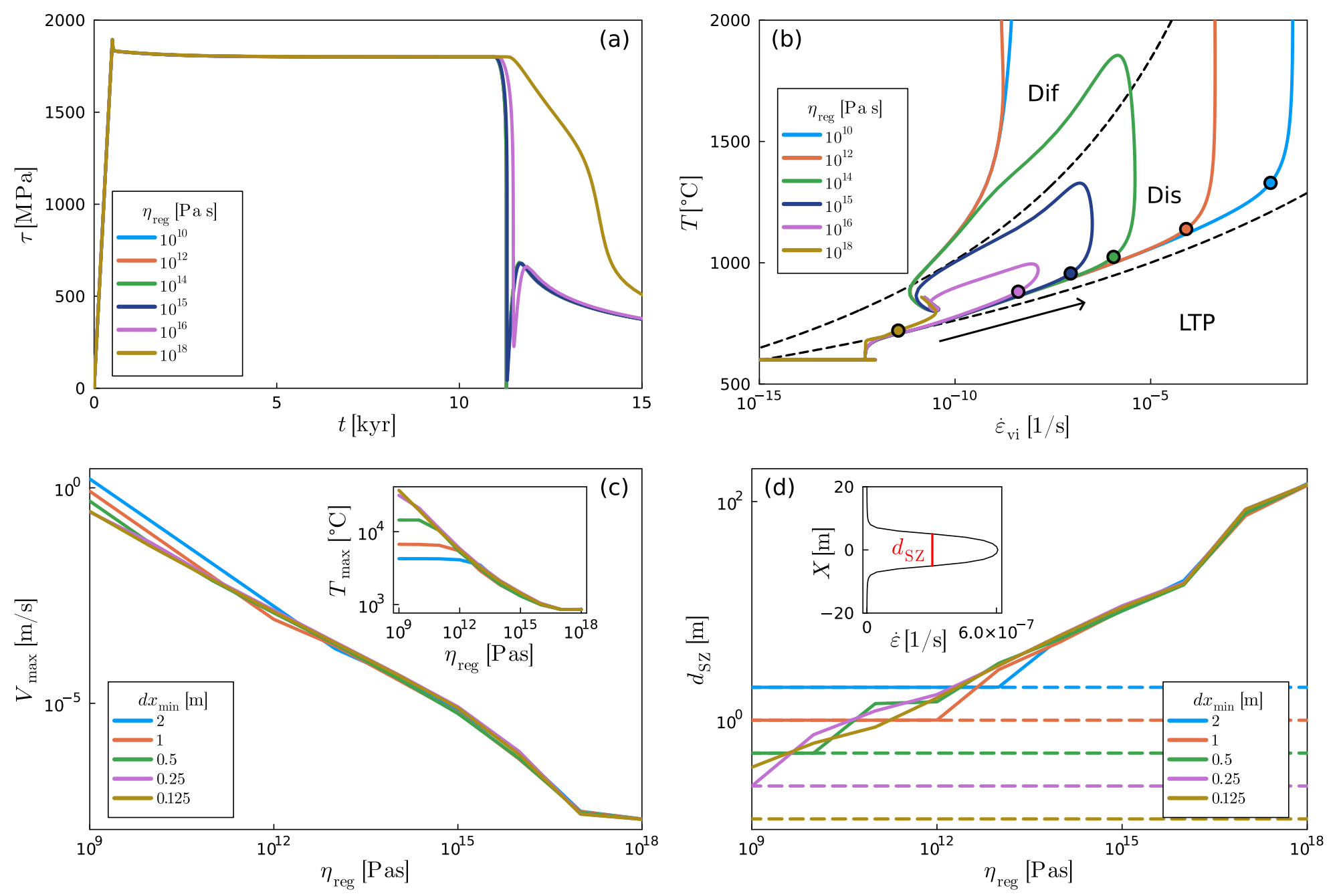
(a)
τ [MPa]
t [kyr]
η_{reg} [Pa s]
10^{10}
10^{12}
10^{14}
10^{15}
10^{16}
10^{18}
(b)
T [°C]
$\dot{\varepsilon}_{\mathrm{vi}}$ [1/s]
Dif
Dis
LTP
(c)
V_{max} [m/s]
η_{reg} [Pas]
T_{max} [°C]
dx_{min} [m]
2
1
0.5
0.25
0.125
(d)
d_{SZ} [m]
X [m]
$\dot{\varepsilon}$ [1/s]
6.0×10⁻⁷

Figure_5.

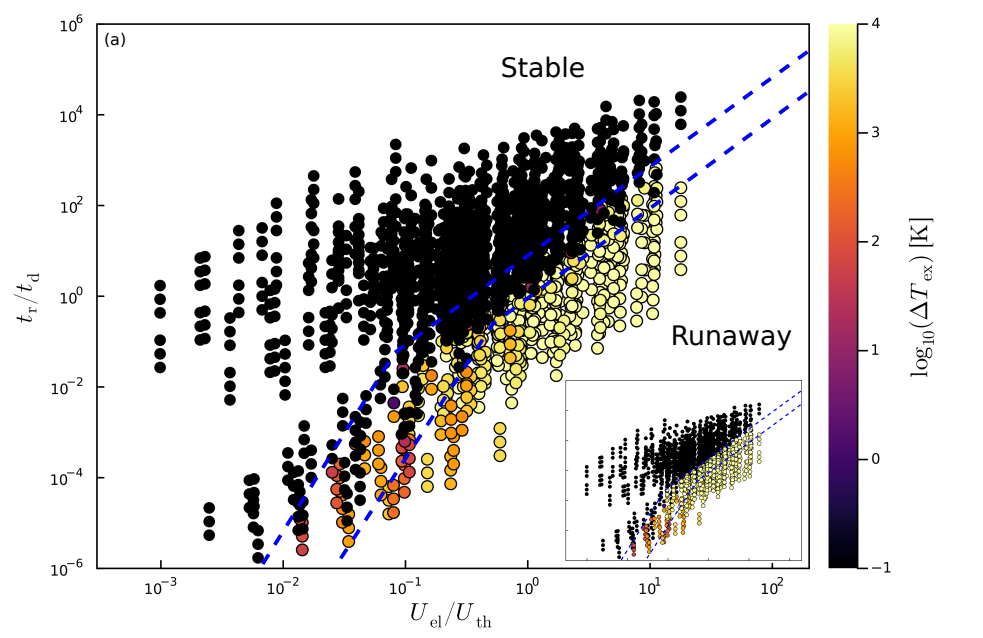
(a)
Stable
Runaway
t_r/t_d
U_{el}/U_{th}
$\log_{10}(\Delta T_{ex})$ [K]

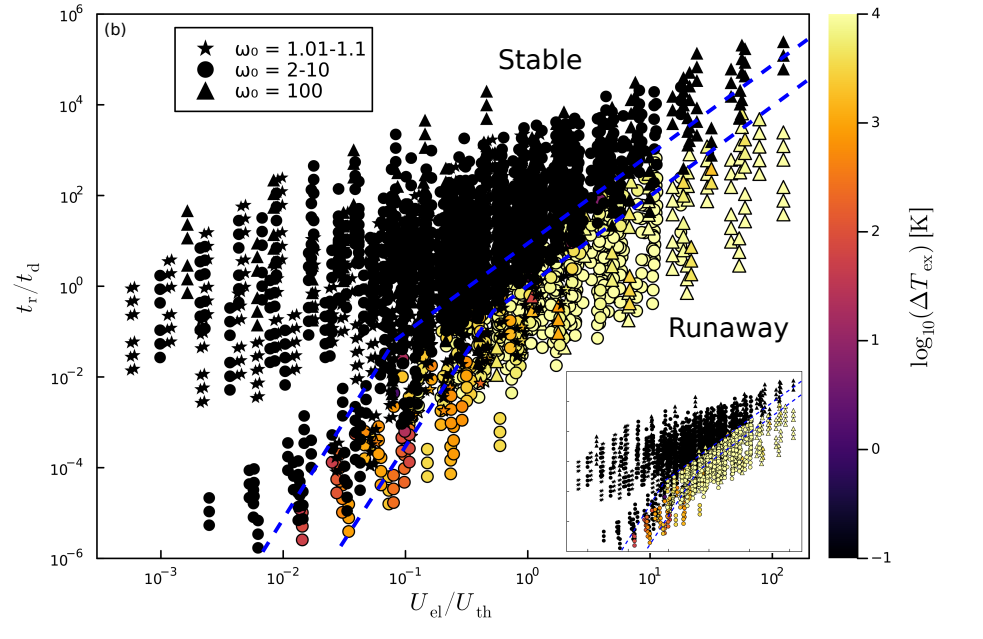
(b)
ω₀ = 1.01-1.1
ω₀ = 2-10
ω₀ = 100
Stable
Runaway
t_r/t_d
U_{el}/U_{th}
$\log_{10}(\Delta T_{ex})$ [K]

Figure_6.

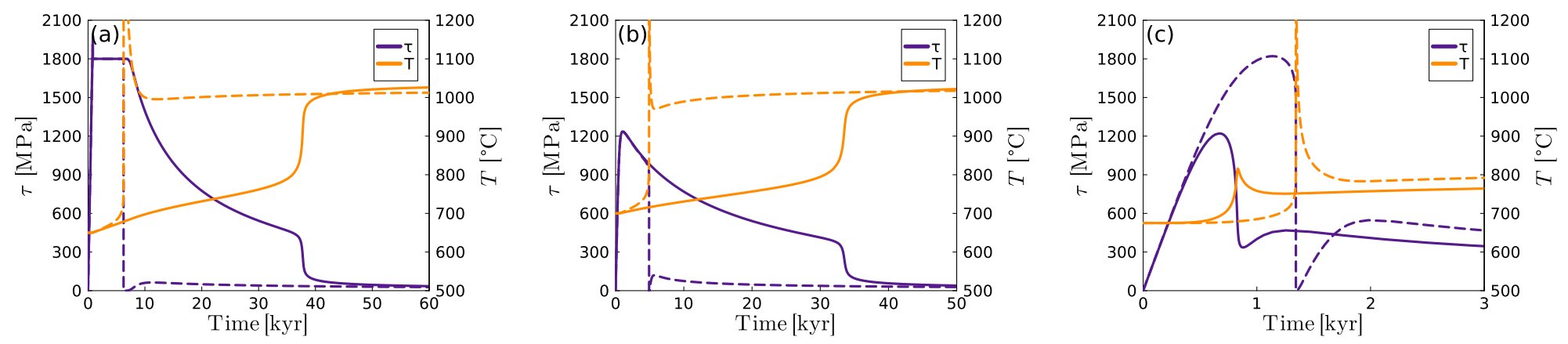
(a)
(b)
(c)
τ
T
τ [MPa]
T [°C]
Time [kyr]